KUNGL
TEKNISKA
HÖGSKOLAN

Simulation of Consolidation Processes by Eulerian Two-Fluid Models

Katarina Gustavsson

Licentiate's Thesis
Royal Institute of Technology
Department of Numerical Analysis and Computing Science

Akademisk avhandling som med tillstånd av Kungl Tekniska Högskolan framlägges till offentlig granskning för avläggande av teknisk licentiatexamen torsdagen den 10 juni 1999 kl 10.00 i sal D31, Lindstedtsvägen 5, Kungl Tekniska Högskolan, Valhallavägen 100, Stockholm.

ISBN 91-7170-419-1

TRITA-NA-9907
ISSN 0348-2952
ISRN KTH/NA/R--99/07--SE

© Katarina Gustavsson, May 1999

Abstract

The objective of this report is to study a model of a gravity and shear induced consolidation process of a dense, flocculated suspension.

The suspension is modeled as a two-constituent mixture of a fluid and solid particles by an Eulerian two-phase fluid model. Both phases are described as incompressible continuous media coupled through an interaction force between the phases.

Constitutive relations for the stresses and the interaction forces in the mixture are fitted to experimental data. The shear-thinning is modeled by a non-constant viscosity that depends on the volume fraction of particles and on the shear rate of the flow. Since the concentration of particles in the mixture is high, irreversible inter-particle forces are also included in the model.

A numerical solver for one and two dimensional problems is designed using finite difference methods both in time and space. To investigate the influence of shear and viscosity on the process a number of simulations are performed.

In the 1D case, the suspension is confined in a closed box and consolidates due to a constant gravity field directed toward the bottom. Conclusions from mathematical analysis are verified by calculations and shows that the size of the viscosity is important for the time scale of the problem. We also show that our results in 1D are consistent with other work done on this subject.

To study the influence of shear and viscosity on the consolidation speed 2D simulations are performed. Shear is induced on the suspension by a movement of the bottom wall with a constant speed. Experiments show that the movement does influence the consolidation rate but the observed differences in the numerical experiments were small.

ISBN 91-7170-419-1 • TRITA-NA-9907 • ISSN 0348-2952 • ISRN KTH/NA/R--99/07--SE

Contents

Acknowledgments

I would like to thank my advisors Jesper Oppelstrup and Björn Engquist for their guidance throughout this project. In particular I thank Jesper....

Furthermore, I would like to thank Jon Eiken at Alfa Laval Separation AB for providing us with experimental data and for many inspiring discussions.

Financial support has been provided by the Parallel Scientific Computing Institute (PSCI) and is greatfully acknowledged.

Chapter 1

Introduction

Sedimentation or consolidation is a separation technique used in many industrial processes such as dewatering of e.g. paper pulp, municipal waste-water sludge and mineral tailings.

In this report we formulate and investigate numerically a mathematical model of a one and two-dimensional consolidation process of a highly concentrated, flocculated suspension of solid particles in a viscous fluid. In a flocculated suspension, the particles are able to attach to each other and form larger clusters called flocs. When the suspension is subjected to sufficiently strong compression, e.g. a gravity field, the liquid is separated from the solid phase and a consolidation process is said to have occurred.

To model the behavior of such a suspension mathematically we use an Eulerian two-phase fluid model. The suspension is then treated as a two-constituent mixture of solid particles and a fluid. Both phases are described as incompressible continua assumed to satisfy averaged equations of motion. This means that for each phase, conservation of mass and of momentum are formulated as partial differential equations. The phases are coupled through the inter-phase momentum transfer. A scalar volume fraction field denoted by ϕ is introduced for the proportion of the total volume occupied by particles. This model is briefly discussed in Section 2. For details and derivation, see for example [9] or [14].

This two-phase model is used for numerical simulations in a variety of different applications and materials such as fluidized beds, [10], dewatering of fiber suspensions, [25] and for flocculated suspensions, [24]. In the application of centrifugal and gravity separation this model is discussed in detail in [23]. Also, the classical one dimensional consolidation model can be derived from this model and is discussed with various applications in [2], [8] and more recently in [5] among others.

As in the case with the equations of motion for an ordinary one phase fluid (cf Navier Stokes equation) the model has to be supplemented with constitutive relations. They should describe the properties of the suspension and adapt the model to a specific application.

We are mainly concerned with three relations to characterize the suspension: the viscosity, the yield stress and the permeability.

Firstly, many concentrated suspensions are known to be shear-thinning, [13]. The viscosity decreases with an increase in shear rate, and is also strongly dependent on the

concentration of particles. Therefore we need to model the variation of the viscosity with concentration and shear rate. Secondly, in dense suspension inter-particle forces must be considered. These forces, related to the yield stress, are assumed to depend on the concentration only, [3]. Thirdly, we consider the interaction force between the phases which is related to the permeability of the suspension. These relations are discussed in Section 2.4.

The issue of the present work is to investigate and perform numerical simulations of a specific consolidation process concerning dewatering of sludge using experimental data on industrial sludge provided by Alfa Laval Separation AB. Specifically, the effects on the consolidation process when the suspension is subjected not only to a gravity field but also to shear are of interest.

As a model problem we consider a closed container with a suspension which consolidates due to gravity. Movement of the bottom wall induces a two dimensional effect of shear on the suspension, see Figure1.1

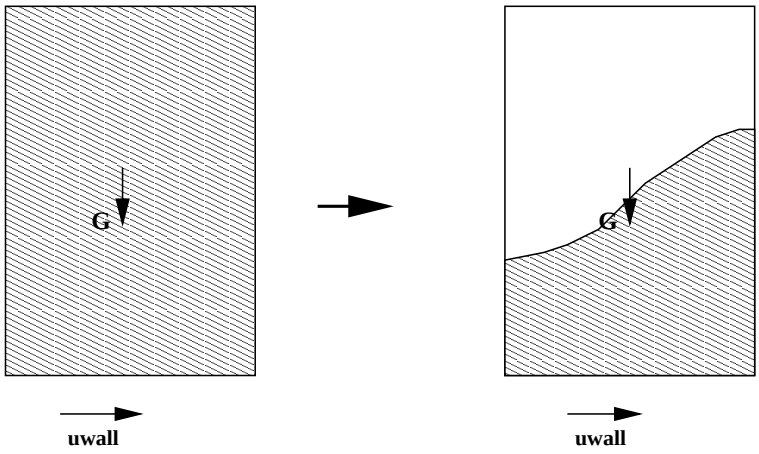

Figure 1.1. Setup for studying the consolidation process. Closed container with a bottom wall moving to the right with a given velocity.

A numerical solver for this test problem is designed based on finite difference methods in both time and space.

When the bottom wall is fixed the suspension consolidates due to gravity only. In the classical 1D consolidation model, [2], [8] and [5], viscous stresses in the model are neglected. Our results show that if the viscous forces are large enough in relation to the inter particle forces they can influence the time scale of the problem. We also show that our numerical results for the 1D problem are consistent with other solutions of this problem, [8].

To investigate the influence of shear on the consolidation process we perform numerical experiments in 2D where we let the bottom wall move with different speeds.

The numerical methods and results are discussed in Chapter 4 and Chapter 5.

Chapter 2

Formulation of the Model

In this section the mathematical model is presented as well as the constitutive relations needed to characterize the suspension. We also discuss a non-dimensional formulation of the equations.

2.1 Two-phase Flow

Models for the flow of a fluid with dispersed particles or flocs can be formulated in a number of different ways depending on for instance the application and whether the suspension is dilute or dense.

In the case of a dilute suspension there are only a few particles suspended in the liquid. If the interaction between the particles is weak a Lagrangian model for the particulate phase can be used. By solving Newtons law of motion, each particle is kept track of in the flow of the continuous phase.

In a dense suspension the interaction between the particles and between the phases have to be considered. A Lagrangian model would not be practical since the effort to keep track of every particle would be too large.

If the length scales related to the flow process are much larger than the microscopic length scales related to the suspension, e.g. a typical particle size, it is sufficient to describe each phase as a continuous medium. The local instantaneous conservation equations for mass, momentum and energy supplemented with jump conditions at the interfaces between the fluid and particles are averaged over each field to produce a multi-phase model. The averaging can be done in space, time or over an ensemble.

2.2 Eulerian Two-Fluid Model for a Concentrated Suspension

We start from an Eulerian two-fluid model obtained by the averaging technique mentioned above. The following assumptions are made

- Both phases are incompressible

- No mass transfer between the phases
- Surface tensions between the phases are neglected

This model is formulated and discussed in e.g. [9] and [10].

$$\begin{aligned}
\phi_t &= -\nabla \cdot (\phi \boldsymbol{u}) && (2.1)\\
0 &= \nabla \cdot (\phi \boldsymbol{u} + (1-\phi)\boldsymbol{v}) && (2.2)\\
\rho_s \phi \frac{D\boldsymbol{u}}{Dt} &= -\phi \nabla p_f - \nabla p_s + \nabla \cdot (\phi \boldsymbol{\tau}_s) + \rho_s \phi \boldsymbol{g} + \boldsymbol{m} && (2.3)\\
\rho_f (1-\phi) \frac{D\boldsymbol{v}}{Dt} &= -(1-\phi)\nabla p_f + \nabla \cdot [(1-\phi)\boldsymbol{\tau}_f] + \rho_f (1-\phi)\boldsymbol{g} - \boldsymbol{m} && (2.4)\\
\frac{D\boldsymbol{u}}{Dt} &= (\boldsymbol{u}_t + \boldsymbol{u} \cdot \nabla \boldsymbol{u}), \quad \text{similarly for } \boldsymbol{v}
\end{aligned}$$

where subscript s is for the solid phase and f is for the fluid phase. Here $\phi \in \mathbb{R}$ is the volume fraction of solids, $\boldsymbol{u}, \boldsymbol{v} \in \mathbb{R}^2$ are the velocities of the particles and of the fluid. $\boldsymbol{\tau} \in \mathbb{R}^{2\times 2}$ denote the stress tensors and $\boldsymbol{m} \in \mathbb{R}^2$ is the inter-phase momentum transfer term. $p_f, p_s \in \mathbb{R}$ are the fluid pressure and the inter particle pressure. ρ_p and ρ_f are the constant densities of the two phases.

Stress-strain relations in each phase are required to close the system as well as an expression of the inter-phase momentum transfer. This term arises due to the relative motion between the particles and the fluid and we take according to [1] and [2],

$$\boldsymbol{m} = (1-\phi)\alpha(\phi)(\boldsymbol{v}-\boldsymbol{u}) + \rho_f \phi C(\phi) \frac{d}{dt}(\boldsymbol{v}-\boldsymbol{u}) \tag{2.5}$$

The first term represents a drag force with a drag coefficient $\alpha(\phi)$. $\alpha(\phi)$ is related to the permeability of the material $k = k(\phi)$ and the viscosity of the fluid, μ as

$$\alpha = \frac{\mu}{k(\phi)} = \frac{1}{D(\phi)} \tag{2.6}$$

D is called the Darcy coefficient.

The second term in equation (2.5) is a virtual mass force proportional to the accelerated mass of fluid by a particle in motion. C is called the virtual mass coefficient.

The stress tensor in the fluid is modeled as a Newtonian stress tensor for an incompressible fluid

$$\boldsymbol{\tau}_f = \mu(\nabla \boldsymbol{v} + \nabla \boldsymbol{v}^T) \tag{2.7}$$

The solid phase is assumed to support shear forces only when velocity gradients are present, i.e. in this respect behave like a fluid,

$$\boldsymbol{\tau}_s = 2\eta_s(\dot{\boldsymbol{\gamma}}(\boldsymbol{u}) - \frac{1}{3}\nabla \cdot \boldsymbol{u}\boldsymbol{I}) \tag{2.8}$$

This is similar to a Newtonian stress tensor with the exception that the viscosity in the particulate phase, η_s depends on the shear rate $\dot{\gamma}$ and the volume fraction ϕ.

$$\eta_s = \eta_s(\phi, |\dot{\boldsymbol{\gamma}}|).$$

The rate of strain tensor is defined as

$$\dot{\boldsymbol{\gamma}}(\boldsymbol{u}) = \frac{1}{2}(\nabla \boldsymbol{u} + \nabla \boldsymbol{u}^T) \tag{2.9}$$

and the shear rate, $|\dot{\gamma}|$ is a scalar formed from the invariants of the rate of strain tensor

$$|\dot{\boldsymbol{\gamma}}| = \sqrt{\frac{1}{2}|(tr\dot{\boldsymbol{\gamma}})^2 - tr(\dot{\boldsymbol{\gamma}} \cdot \dot{\boldsymbol{\gamma}})|}$$

$$tr\dot{\boldsymbol{\gamma}} = \sum_n (\dot{\boldsymbol{\gamma}})_{nn}$$

The experimental data available for the viscosity of a suspension is the apparent (mixture) viscosity, η_{mix}. In a suspension the mixture viscosity increases with the solids volume fraction. In the material studied, at high concentrations, the viscosity of the mixture will be orders of magnitude larger than the fluid viscosity. We will therefore neglect $\boldsymbol{\tau}_f$ and assume

$$\eta_{mix} = \phi \eta_s$$

This relation together with (2.9) leads to the following expression for the stress tensor $\boldsymbol{\tau}_s$

$$\boldsymbol{\tau}_s = \frac{\eta}{\phi}(\nabla \boldsymbol{u} + \nabla \boldsymbol{u}^T - \frac{2}{3}\nabla \cdot \boldsymbol{u}\boldsymbol{I}) \tag{2.10}$$

This simplification will not be valid in the clear fluid limit but its influence in the compression zone will most likely be of little importance.

Making use of the assumptions discussed above and with (2.6) and (2.10) inserted in (2.3) and (2.4) we finally obtain

$$\phi_t = -\nabla \cdot (\phi \boldsymbol{u}) \tag{2.11}$$

$$0 = \nabla \cdot (\phi \boldsymbol{u} + (1-\phi)\boldsymbol{v}) \tag{2.12}$$

$$\begin{aligned} \rho_s \phi \frac{D\boldsymbol{u}}{Dt} =& -\phi \nabla p_f - \nabla p_s + \nabla \cdot [\eta(\nabla \boldsymbol{u} + \nabla \boldsymbol{u}^T - \frac{2}{3}\nabla \cdot \boldsymbol{u}\boldsymbol{I})] \\ &+ \rho_s \phi \boldsymbol{g} + \frac{1-\phi}{D(\phi)}(\boldsymbol{v} - \boldsymbol{u}) + \rho_f \phi C(\phi)\frac{d}{dt}(\boldsymbol{v} - \boldsymbol{u}) \end{aligned} \tag{2.13}$$

$$\begin{aligned} \rho_f (1-\phi)\frac{D\boldsymbol{v}}{Dt} =& -(1-\phi)\nabla p_f + \rho_f (1-\phi)\boldsymbol{g} \\ &- \frac{1-\phi}{D(\phi)}(\boldsymbol{v} - \boldsymbol{u}) - \rho_f \phi C(\phi)\frac{d}{dt}(\boldsymbol{v} - \boldsymbol{u}) \end{aligned} \tag{2.14}$$

By scaling analysis, this model can be further simplified by neglecting inertial forces and virtual mass forces as discussed below.

2.3 Dimensionless Formulation

A dimensionless formulation of the equations provides indicative parameters, insight about the relative size of different terms and their relative importance.

Define the following dimensionless variables for the consolidation process in a $H \times H$ box under $\boldsymbol{g}$ gravity.

Length $x_i^* = x_i/H$

Velocity $\boldsymbol{u}^* = \boldsymbol{u}/U_0$ and $\boldsymbol{v}^* = \boldsymbol{v}/U_0$

Time $t^* = t/T$

Density $\rho^* = \rho/\Delta\rho, \quad \Delta\rho = \rho_s - \rho_f$

Liquid pressure $p_f^* = p_f/P$

Gravity $\mathbf{e}^*{}_g = \boldsymbol{g}/G$

where * denotes dimensionless variables and we will rapidly drop the *.

The velocity scale U_0 is the free settling velocity of an individual floc at concentration ϕ_0 in the absence of any inter-particle forces. U_0 is related to the permeability of the material as

$$U_0 = \Delta\rho G D_0$$

where $D_0 = k_0/\mu$ is a characteristic Darcy coefficient of the material. The notation P_{s0} is used for a characteristic interparticle pressure, η_0 for the viscosity and C_0 for the virtual mass coefficient.

If the convective time scale of the problem is used as a characteristic time, $T = \frac{H}{U_0}\ T$ is the time it takes for a single floc to settle from the top to the bottom of the container.

Making use of the parameters, equation (2.13) can be written in dimensionless form as

$$\frac{U_0^2}{GH}\rho_s\phi\frac{D\boldsymbol{u}}{Dt} = -\frac{P}{GH\Delta\rho}\phi\nabla p_f - \frac{P_{s0}}{GH\Delta\rho}\nabla p_s + \frac{U_0\eta_0}{GH^2\Delta\rho}\nabla\cdot(\phi\boldsymbol{\tau}_s) + \rho_s\phi\boldsymbol{e}_g + \frac{1-\phi}{D(\phi)}(\boldsymbol{v}-\boldsymbol{u}) + \frac{U_0^2 C_0}{GH}\phi C(\phi)\frac{d}{dt}(\boldsymbol{v}-\boldsymbol{u})$$

where

$$\tau_0 = \frac{U_0\eta_0}{H}$$

An appropriate scale for the pressure must be chosen in different ways depending on the application. If the sedimentation process is dominated by gravity it is natural to let the pressure term balance the gravitational forces by

$$P = \Delta\rho G H$$

Then

$$F^2\rho_s\phi\frac{D\boldsymbol{u}}{Dt} = -\phi\nabla p_f - \frac{1}{Pe}\nabla p_s + \frac{1}{Pe_s}\nabla\cdot(\phi\boldsymbol{\tau}_s)$$
$$+\rho_s\phi\boldsymbol{e}_g + \frac{1-\phi}{D(\phi)}(\boldsymbol{v}-\boldsymbol{u}) + F^2C_0\phi C(\phi)\frac{d}{dt}(\boldsymbol{v}-\boldsymbol{u}) \tag{2.15}$$

where the following dimensionless numbers are introduced, see also [24]

$$Pe = \frac{G\Delta\rho H}{P_{s0}} \qquad Pe_s = \frac{G\Delta\rho H}{\tau^0} \qquad F^2 = \frac{U^2}{GH}.$$

Pe and Pe_s are Peclet numbers which relate compression and shear strength of the material to the gravitational force. They can be viewed as a relation between the parameters related to the process and the material properties, yield pressure and shear strength. The Froude number, F^2, is the ratio of the inertia force to the gravity force.

Equation (2.15) has terms of the order

$$F^2 \qquad \frac{1}{Pe} \qquad \frac{1}{Pe_s} \qquad 1$$

Since F is based on the slow sedimentation velocity, U_0, F^2 will be a small parameter. This assumption will be investigated using experimental data,see Section 2.5. If $C_0 \leq \mathcal{O}(1)$ all the inertial terms can be neglected in the equations giving

$$-\phi\nabla p_f + \frac{1}{Pe_s}\nabla\cdot(\phi\boldsymbol{\tau}_s) = \frac{1}{Pe}\nabla p_s - \frac{1-\phi}{D(\phi)}(\boldsymbol{v}-\boldsymbol{u}) - \rho_s\phi\boldsymbol{e}_g \tag{2.16}$$

In the same way (2.11), (2.12) and (2.14), after neglecting the inertial terms, can be written in dimensionless form as

$$\phi_t = -\nabla\cdot(\phi\boldsymbol{u}) \tag{2.17}$$
$$\nabla\cdot(\phi\boldsymbol{u} + (1-\phi)\boldsymbol{v}) = 0 \tag{2.18}$$
$$-(1-\phi)\nabla p_f = \frac{1-\phi}{D(\phi)}(\boldsymbol{v}-\boldsymbol{u}) - \rho_f(1-\phi)\boldsymbol{e}_g \tag{2.19}$$

Add (2.16) and (2.19) in order to get

$$\frac{1}{Pe}\nabla p_s - \frac{1}{Pe_s}\nabla\cdot(\phi\boldsymbol{\tau}_s) = -\nabla p_f + (\rho_s\phi + \rho_f(1-\phi))\boldsymbol{e}_g \tag{2.20}$$

and use (2.20) in (2.16) to get a relation between u and v.

$$\boldsymbol{v} = \boldsymbol{u} - D(\nabla p_f - \rho_f\boldsymbol{e}_g) \tag{2.21}$$

This expression can be used in (2.18) in order to eliminate the fluid velocity, giving the following coupled hyperbolic-elliptic system to be solved for the unknowns ϕ, p and $\boldsymbol{u}$.

$$\phi_t + \nabla\cdot(\phi\boldsymbol{u}) = 0 \tag{2.22}$$
$$\nabla\cdot(\boldsymbol{u} - (1-\phi)D(\phi)\nabla p) = 0 \tag{2.23}$$
$$-\nabla p + \frac{1}{Pe_s}\nabla\cdot(\phi\boldsymbol{\tau}_s) = \frac{1}{Pe}\nabla p_s - \phi\boldsymbol{e}_g \tag{2.24}$$

where $p = p_f - p_0 - \rho_f \boldsymbol{e}_g \cdot \mathbf{x}$ is the reduced pressure.

Notice that if $D(\phi) = k(\phi)/\mu \to 0$ equation (2.21) yields that $\boldsymbol{u} = \boldsymbol{v}$ and equation (2.23) that $\nabla \cdot \boldsymbol{u} = 0$. Since $\frac{D\phi}{Dt} = -\phi \nabla \cdot \boldsymbol{u}$ there will then be no separation of the phases. The size of the permeability can be regarded as a measure of the ability to separate the solid phase from the liquid phase. We also look into the influence of the bulk viscosity η on the dewatering, see Section 3.2.1.

2.4 Constitutive Relations

The constitutive laws are necessary to form a closed set of equations and to accomplish the characterization of the material. The basis for this work has been that the material data needed should be furnished by techniques which can be applied routinely. There are traditional devices using pressure filtration and piston experiments in 1D-settings for determining permeability and force-deformation relationships. Various types of rotating and oscillatory viscosimeters can be used to determine the shear behavior. The recent dissertation [12] gives an overview of a number of techniques developed for mineral applications. It proposes the yield pressure and the "hindered settling factor" - the latter related to the permeability - as important characteristics. The work gives ample illustration of the experimental difficulties and how some of these can be overcome.

Usually the experimental apparatus is limited to a certain range of the parameters. In particular, the industrial sludge studied in this work has very low permeability and standard filter press devices require too long times to be practically useful.

A more fundamental problem is the determination of volume fraction solids. This is easy for mineral suspensions where the density of the solids is accurately known, but we have not found any experimental technique which can measure this quantity for organic sludge. Solids weight fraction, however, is easily determined by drying, and it has been necessary to convert this to solids volume fraction by assumptions on intra-cellular water content.

In what follows we assume that the models determined by 1D devices are also valid in the 2D case.

Below, we discuss the constitutive relations that are used in the simulations. They are fitted to experimental data on industrial sludge provided by Alfa Laval Separation AB.

2.4.1 Permeability

The interaction between the phases is due to drag forces on the particles or flocs when transported through the fluid. To describe this we use the concept of permeability from the theory of flow through porous media [18]. The permeability, k has the dimension $[m^2]$ so $\sqrt{k}$ is a length scale representative of some pore diameter. We assume that the medium is isotropic.

The sludge experimental data were fitted to a power law function of ϕ.

$$D(\phi) = \frac{k(\phi)}{\mu} = K_D \phi^{n_D} \tag{2.25}$$

where $K_D = 4.6 \cdot 10^{-18} m^2/Pas$ and $n_D = -7.41$. Note the extreme variation of the sludge permeability, Figure 2.1. The model has to be modified in the limit $\phi \to 0$: as $\phi \to 0$ the fall speed of a single floc should appear, see Section 3.1.

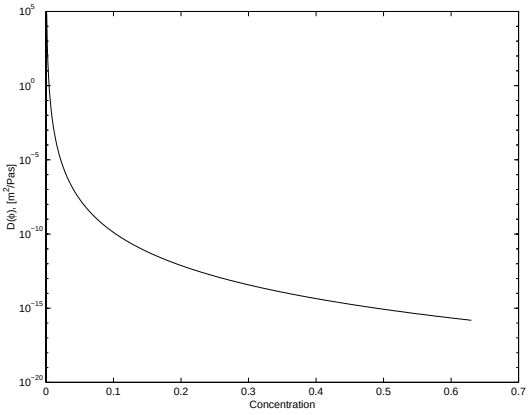

Figure 2.1. $D(\phi) = \frac{k}{\mu}$ as a function of ϕ for the sludge experimental data

2.4.2 Yield Pressure

In a flocculated suspension the particles attract each other. In a strongly flocculated suspension the interparticle attraction forces are strong enough to overcome Brownian motions so that the particles attach to each other and form flocs. For a volume fraction ϕ higher than the so called gel forming fraction the structure is changed from individual flocs to a porous network of particles filled with fluid. The network is able to support stresses and resist compression until the compressive force exceeds a volume fraction dependent yield pressure . Then there will be an irreversible compression of the network resulting in fluid being released and an increase in concentration of solid particles. The yield pressure is assumed to increase with concentration and the network will be able to support a higher compression force. The change is irreversible: when the external compression load decreases, the suspension will not revert to its original volume fraction.

To model the irreversibility effects we follow the method introduced in [24]. Since

$$\frac{D\phi}{Dt} = \phi_t + \boldsymbol{u} \cdot \nabla\phi = -\phi \nabla \cdot \boldsymbol{u}$$

the sign of $\nabla \cdot \boldsymbol{u}$ determines whether the suspension is under compression (ϕ is increasing) or dilation (ϕ is decreasing) along a particle path. Whenever ϕ is decreasing the yield pressure should drop rapidly to zero, and not until ϕ reaches the same level as before the decrease, it increases to the same level again, see figure 3.

The maximal ϕ encountered since $t = 0$ by a material particle, $\phi^*(\boldsymbol{x}, t)$, satisfies

$$\frac{D\phi^*}{Dt} = \begin{cases} \frac{D\phi}{Dt} & \text{when } \phi \geq \phi^*, \ \frac{D\phi}{Dt} > 0, \\ 0 & \text{otherwise.} \end{cases} \tag{2.26}$$

When ϕ decreases, and until it reaches its old maximum value again, this is a pure advection of ϕ^* by the velocity field $\boldsymbol{u}$. Otherwise $\phi^* = \phi$, see Figure 2.2.

To obtain the above mentioned effects of the irreversibility let p_s be a function of ϕ and ϕ^* as

$$p_s(\phi, \phi^*) = \begin{cases} 0 & \text{if } \phi < \phi^*, \\ p_{s,yield} & \text{if } \phi \geq \phi^*. \end{cases} \tag{2.27}$$

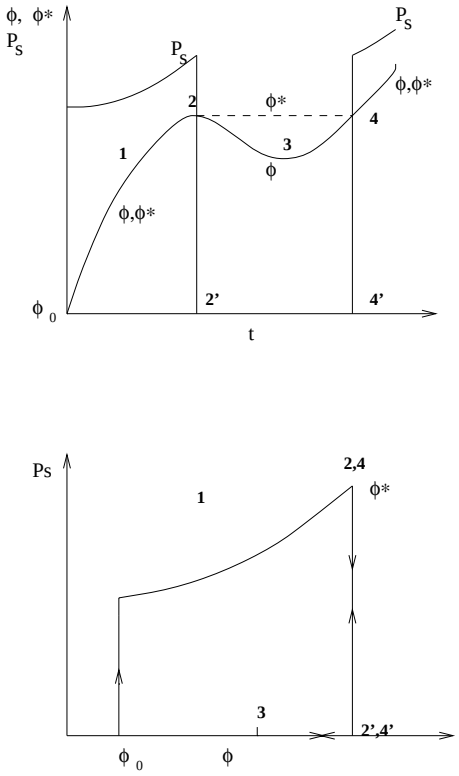

Figure 2.2. Irreversibility effects modeled using ϕ^*. The upper figure describes how ϕ is changing along a particle path and how the yield pressure is increasing with increasing ϕ. As soon as ϕ begins to decrease the yield pressure drops to zero.

As in the case with the permeability function, we assume a power law behavior of the yield pressure as a function of the concentration, see Figure 2.3

$$p_{s,yield}(\phi) = K_y \phi^{n_y} \tag{2.28}$$

where $K_y = 5 \cdot 10^6 \ Pa$ and $n_y = 4.846$.

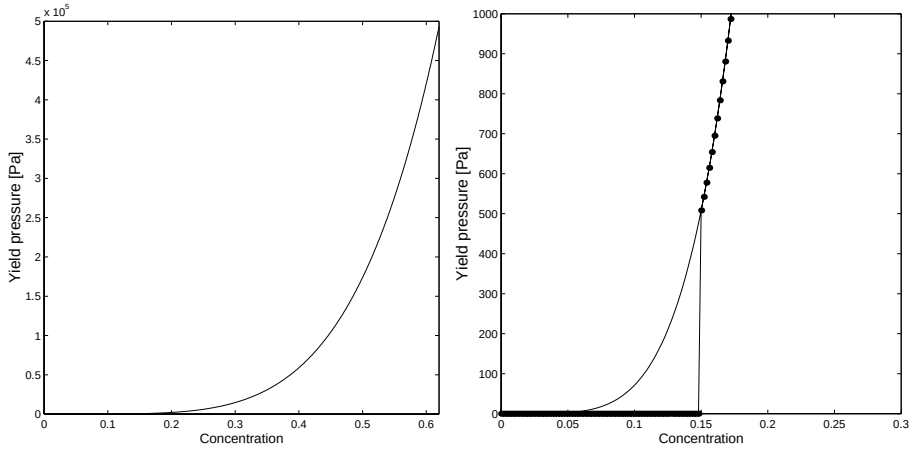

(a) Loading

(b) Loading and unloading

Figure 2.3. Yield pressure as a function of ϕ fitted to experimental data. In the right figure there is unloading at $\phi^* = 0.15$ (dotted line).

2.4.3 Viscosity

Flocculated suspensions exhibit so-called non-Newtonian behavior. They are often strongly shear thinning, with viscosity decreasing with an increasing shear rate. A treatment of rheological behavior of suspensions can be found in [3] and [13]. At low shear rates the flocs are assumed not to break and the viscosity is essentially constant, called the lower Newtonian region. At higher shear rates the flocs deform and begin to break down. The velocity gradients induce an orientation of the floc structure to form layers separated by clear fluid. This will cause the apparent viscosity to decrease and the suspension will be shear thinning. For high enough shear rate the viscosity will again reach a region with constant viscosity but at a lower level, the upper Newtonian level.

The viscosity is also strongly increasing with the volume fraction of particles.

Experimental data for the viscosity as a function of shear rate show a power law behavior and have been fit to the Carreau-Yasuda model [4], see Figure 2.4,

$$\frac{\eta - \eta_\infty}{\eta_0 - \eta_\infty} = (1 + (\lambda\dot{\gamma})^a)^{(n-1)/a} \tag{2.29}$$

Here η_0 is the zero shear rate viscosity (lower Newtonian region) and η_∞ is the upper Newtonian region. n is called the power law exponent, $n > 0$. The upper and lower regions are not well determined by available experimental data. The measurements were conducted at shear rates where the viscosity was still dependent on the shear rate. η_0 and η_∞ are treated as somewhat adjustable parameters for which only order of magnitude estimates are available. This model is combined with a volume fraction dependence as:

$$\eta(\phi, |\dot{\boldsymbol{\gamma}}|) = 9.15 \cdot 10^7 \phi^{3.4} \left(1 + \frac{|\dot{\boldsymbol{\gamma}}|}{0.05}\right)^{-0.9} \tag{2.30}$$

Note that $n > 0$ is necessary for the model to be reasonable. With n=0.1 the flow behaves almost like a Bingham fluid with a shear rate independent critical shear stress.

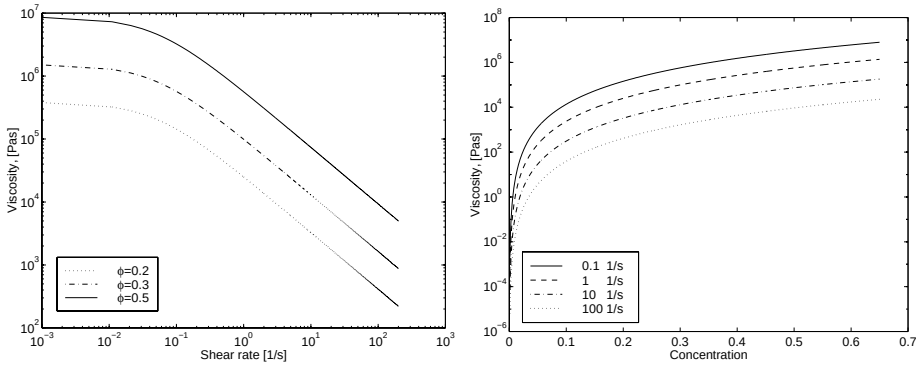

(a) $\eta(|\dot{\boldsymbol{\gamma}}|)$ for different values of ϕ (b) $\eta(\phi)$ for different values of $|\dot{\boldsymbol{\gamma}}|$

Figure 2.4. Viscosity as a function of the shear rate $|\dot{\boldsymbol{\gamma}}|$ for different values of ϕ.

2.5 Indicative Froude and Peclet numbers

With the above discussed constitutive models, the dimensionless numbers introduced in subsection (2.3) can be determined and we can motivate the fact that we neglect the inertial terms.

As a reference state we choose $\phi = \phi_0 = 0.1$ which is the initial volume fraction of particles in the suspension. Using equations (2.25) and (2.28) we obtain

$$D_0 = D(\phi_0) = 1.2 \cdot 10^{-10}\ m^2/Pas$$

and

$$P_{s0} = P_s(\phi_0) \approx 70\ Pa$$

Note that D_0 and P_{s0} are related only to the properties of the material and not to the specific process the suspension is subjected to.

From equation (2.30) the reference value of the viscosity, η_0 is computed as

$$\eta_0 = \eta(\phi_0, u_{wall}/H)$$

where we use u_{wall}/H as a measure of the shear rate. By using the relation between the sedimentation velocity, U_0 and the permeability: $U_0 = \Delta\rho G D_0$, the dimensionless numbers can be written in the following form

$$Pe = \frac{G\Delta\rho H}{P_{s0}} \quad F^2 = \frac{(\Delta\rho H D_0)^2}{H} \quad Pe_s = \frac{H}{D_0\eta_0}$$

We compute Pe, Pe_s and F^2 for different values of G and u_{wall}, see Table 2.1. In all computations $\Delta\rho = 10^3\ kg/m^3$ and $H = 0.1m$.

$u_{wall}\ [m/s]$	$G\ [m/s^2]$	$1/Pe$	$1/Pes$	F^2
0.001	10^3	$7.1 \cdot 10^{-4}$	$4.0 \cdot 10^{-5}$	$1.7 \cdot 10^{-10}$
	10^4	$7.1 \cdot 10^{-5}$	$4.0 \cdot 10^{-5}$	$1.7 \cdot 10^{-9}$
	10^5	$7.1 \cdot 10^{-6}$	$4.0 \cdot 10^{-5}$	$1.7 \cdot 10^{-8}$
0.01	10^3	$7.1 \cdot 10^{-4}$	$1.7 \cdot 10^{-5}$	$1.7 \cdot 10^{-10}$
	10^4	$7.1 \cdot 10^{-5}$	$1.7 \cdot 10^{-5}$	$1.7 \cdot 10^{-9}$
	10^5	$7.1 \cdot 10^{-6}$	$1.7 \cdot 10^{-5}$	$1.7 \cdot 10^{-8}$
0.1	10^3	$7.1 \cdot 10^{-4}$	$3.0 \cdot 10^{-6}$	$1.7 \cdot 10^{-10}$
	10^4	$7.1 \cdot 10^{-5}$	$3.0 \cdot 10^{-6}$	$1.7 \cdot 10^{-9}$
	10^5	$7.1 \cdot 10^{-6}$	$3.0 \cdot 10^{-6}$	$1.7 \cdot 10^{-8}$

Table 2.1. Dimensionless parameters for different values of the wall speed and the G-number.

As long as u_{wall} and G are chosen in the range given in Table 2.1 the inertial terms can be neglected since F^2 is smaller than both $1/Pe$ and $1/Pe_s$. However, if the G-number or u_{wall} is increased further the terms will eventually be of the same order and the inertial effects have to be considered in the equations.

In the application of sludge dewatering some realistic values on G and u_{wall} are: $G \approx 15000\ m/s^s$ and $u_{wall} \approx 0.02\ m/s$. Most of the numerical computations are performed with $G = 10000m/s^2$ and u_{wall} ranging from $0m/s$ to $0.1m/s$.

Chapter 3

Mathematical Analysis

In this chapter we discuss mathematical features of the one and two dimensional model.

$$\phi_t = -\nabla \cdot (\phi \mathbf{u}) \tag{3.1}$$
$$0 = \nabla \cdot (\mathbf{u} - (1-\phi) D(\phi) \nabla p) \tag{3.2}$$
$$0 = -\nabla p - \nabla(p_s) + \nabla \cdot (\phi \boldsymbol{\tau}_s) + \phi(\rho_s - \rho_f)\mathbf{g} \tag{3.3}$$

where p is the reduced pressure and $\boldsymbol{\tau}_s$ is given by (2.10).

3.1 Characteristics

To simplify the analysis of the equations, to find suitable numerical methods and to be able to compare our results with work done by others [8], [24] we first treat the one dimensional case. This is pure consolidation of the suspension due to gravity, there is no unloading and $\phi^* = \phi$ always.

Let $y \in [0, H]$ where H is the height of the container. With the gravitational force acting in the negative y-direction, the system of equations (3.1)-(3.3) is reduced to

$$\frac{\partial \phi}{\partial t} + \frac{\partial (v\phi)}{\partial y} = 0 \tag{3.4}$$

$$\frac{\partial}{\partial y}\left(\tilde{D}\frac{\partial p}{\partial y}\right) - \frac{\partial v}{\partial y} = 0 \tag{3.5}$$

$$\frac{4}{3}\frac{\partial}{\partial y}(\eta \frac{\partial v}{\partial y}) - \frac{\partial p}{\partial y} = \frac{\partial p_s}{\partial y} + \phi g(\rho_s - \rho_f) \tag{3.6}$$

where $\tilde{D} = D(\phi)(1-\phi)$ and the Darcy coefficient, $D(\phi) = k(\phi)/\mu$. The solid pressure p_s is assumed to be a known function of ϕ. Finally the viscosity of the bulk fluid is a function of ϕ, $\eta = \eta(\phi)$.

Equations (3.5) and (3.6) form an elliptic system of equations for the velocity and pressure. Equation (3.4) is a hyperbolic conservation law for the particle concentration.

As boundary condition we use, $v = 0$ and $\partial p/\partial n = 0$ at $y = 0, H$

Equation (3.5) is integrated to

$$\frac{\partial p}{\partial y} = \frac{v}{\tilde{D}}$$

and equation (3.6) becomes

$$\frac{4}{3}\frac{\partial}{\partial y}(\eta\frac{\partial v}{\partial y}) - \frac{v}{\tilde{D}} = \frac{\partial p_s}{\partial y} + \phi g(\rho_s - \rho_f)$$

In most practical cases $\tilde{D}\eta/H^2 \ll 1$ and for $y \gg \sqrt{\tilde{D}\eta}$ the diffusive term can be neglected compared to the other terms yielding an expression for v as

$$v \approx -\tilde{D}\left(m\phi_y + \phi g(\rho_s - \rho_f)\right), \quad m = \frac{\partial p_s}{\partial \phi} \tag{3.7}$$

With $\hat{D}(\phi) = g(\rho_s - \rho_f)\phi\tilde{D}$ (3.4) becomes a convection-diffusion equation

$$\phi_t - (\hat{D}\phi)_y - \left(\frac{\hat{D}}{g(\rho_s - \rho_f)} m\phi_y\right)_y = 0 \tag{3.8}$$

Equation (3.8) is referred to as the classical 1D model. It is used in many applications and treated from both a mathematical point of view as well as numerical (see for example [2], [5], [7], [8]).

To motivate a numerical scheme for this equation some knowledge of its characteristic behavior is required. This can be obtained from the convective part of the equation

$$\phi_t - (\hat{D}\phi)_y = 0$$

defining the flux function

$$f(\phi) = -\hat{D}\phi.$$

With the permeability function (2.25) the flux function can be written as

$$f(\phi) = -C\phi^2(1-\phi)\phi^{-n_D} = -C(1-\phi)\phi^{-n_D+2} \tag{3.9}$$

where $C = K_D g(\rho_s - \rho_f) \approx 5 \cdot 10^{-14}$ and $K_D = 5 \cdot 10^{-18} m^2/Pas$ and $n_D = -7.41$, see Figure 3.1(a).

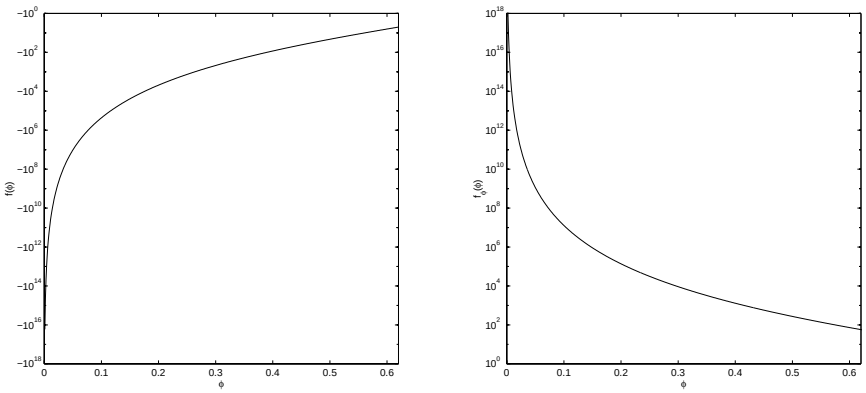

(a) Flux function, $f(\phi)$ (b) ϕ-derivative of f, $f_\phi(\phi)$

Figure 3.1. The flux $f(\phi)$ and the ϕ-derivative of f, $f_\phi(\phi)$ as functions of ϕ, scaled with $1/C_1$.

The slope of the characteristics is given by the ϕ-derivative of the flux function as

$$f_\phi = -(\hat{D} + \phi \hat{D}_\phi)$$

In Fig. 3.1(b) we see that $f_\phi > 0$ for $0 \leq \phi \leq 0.6$. This means that all the characteristics will have a positive slope increasing with ϕ and decreasing y. The characteristics will diverge and the solution will not develop any shocks. Also, both the flux function and its derivative will tend to infinity when the volume fraction ϕ tend to zero. To avoid this we approximate the permeability function for small $\phi \leq \phi_0/2$ with a linear expression with the slope given by the slope of $D(\phi)$ at $\phi = \phi_0/2$, see Figure 3.2.

$$D(\phi) = \begin{cases} K_D \phi^{-n_D} & \text{if} \phi > \frac{\phi_0}{2} \\ K_D (\frac{\phi_0}{2})^{-n_D} (1 - n_D (\phi - \frac{\phi_0}{2}) / \frac{\phi_0}{2}) & \text{if} \phi \leq \frac{\phi_0}{2} \end{cases} \tag{3.10}$$

K_D and n_D as before.

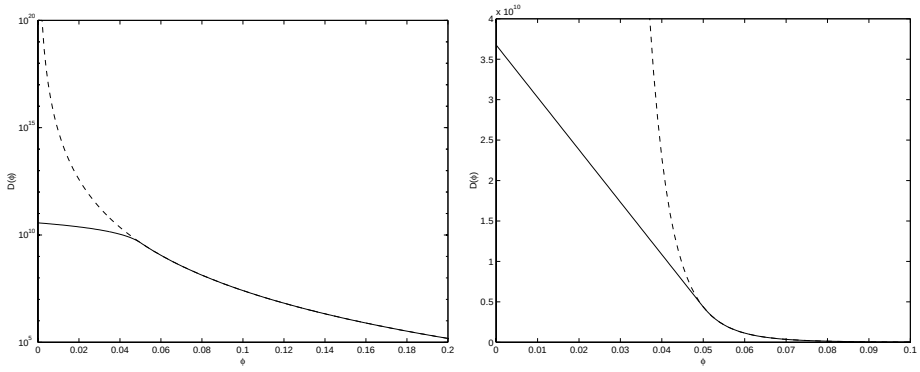

Figure 3.2. Permeability as a function of ϕ. A linear expression is used for small $\phi \leq 0.05$.

This will change the flux function and its ϕ-derivative according to Figure 3.3(a),(b).

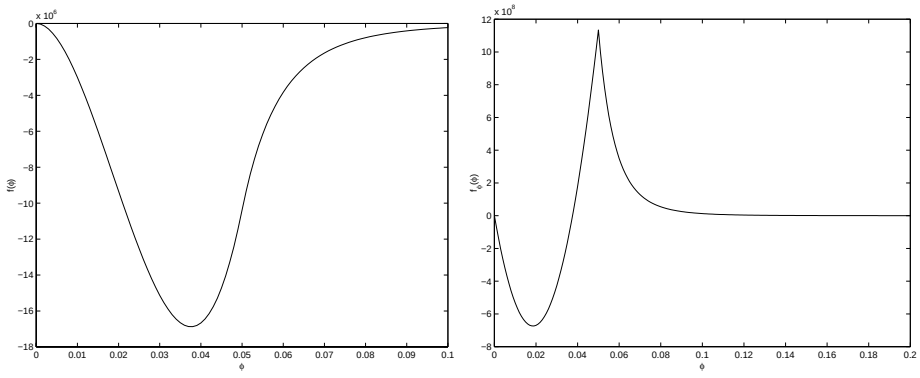

(a) Flux function, $f(\phi)$ (b) ϕ-derivative of f, $f_\phi(\phi)$

Figure 3.3. The flux $f(\phi)$ and the ϕ-derivative of f, $f_\phi(\phi)$ when $D(\phi)$ is used according to (3.10)

The modification of the permeability function produces a non-convex flux function, see Figure 3.3 (a). For small ϕ this implies a complicated shock structure. Nevertheless, numerical experiments presented in Section 5.3 indicate a simple shock between the clear fluid phase and the sediment as we expect.

3.2 Qualitative Behavior of the Solution

We have argued that the constitutive relations i.e. the viscosity, permeability and yield pressure, are important in order to characterize the suspension. This motivates a study of the behavior of the solution in terms of the above mentioned functions.

3.2.1 1D Model

Start from the 1D system given by the equations (3.4)-(3.6). Let $\eta = \eta(\phi)$, $\tilde{D} = \tilde{D}(\phi)$ and $p_s = p_s(\phi)$.

By integrating equation (3.5) the pressure can be eliminated from equation (3.6) and we obtain the following equation for the particle velocity

$$\frac{4}{3}\frac{\partial}{\partial y}(\eta\frac{\partial v}{\partial y}) - \frac{v}{\tilde{D}} = \frac{\partial p_s}{\partial y} + \phi g(\rho_s - \rho_f) \tag{3.11}$$

together with the boundary conditions

$$v(0) = v(H) = 0.$$

Assume that ϕ is bounded but can be discontinuous and that $p_s(\phi) \in C$. Then, if there exists a smooth solution v the following holds:

If $\tilde{D}\eta/H^2 \ll 1$ then

$$\|v\| \leq |\tilde{D}|_\infty(\Delta\rho g\|\phi\| + \|(p_s)_y\|). \tag{3.12}$$

where $\|\cdot\|$ is the usual L_2 norm defined by

$$\|f\|^2 = (f, f) = \int_0^H |f|^2 dy$$

We see that the particle velocity is bounded by the permeability related Darcy coefficient. In 1D the particle velocity is direct related to the time scale of the consolidation process and a small permeability will lead to a slow sedimentation speed.

If η or $\tilde{D}$ becomes large i.e. $\tilde{D}\eta/H^2 \gg 1$ then

$$\|v\| \leq \frac{C}{\eta_{min}}(\Delta\rho g\|\phi\| + \|(p_s)_y\|) \tag{3.13}$$

where $C = 3H^2/16\pi^2$. The velocity is now bounded by $1/\eta_{min}$. This means that when the viscosity becomes large it will eventually influence the sedimentation speed and time scale of the process.

In order to obtain the estimates (3.12) and (3.13), multiply equation (3.11) with v and integrate by parts. Using the Poincaré inequality

$$\|v_y\|^2 \geq \frac{4\pi^2}{H^2}\|v\|^2$$

yields

$$\|v\| \leq \frac{\Delta\rho g\|\phi\| + \|(p_s)_y\|}{\frac{1}{|\tilde{D}|_\infty} + \frac{16}{3}\frac{\pi^2}{H^2}\eta_{min}} \tag{3.14}$$

where

$$\eta_{min} = \min_{0\leq y\leq H} \eta(y)$$

When $\tilde{D}\eta/H^2 \ll 1$ we obtain (3.12) and when $\tilde{D}\eta/H^2 \gg 1$ we obtain (3.13).

The fact that the time scale of the process is influenced by the size of the viscosity is validated by performing numerical experiments in 1D. The results are reported in Section 5.3.

3.2.2 2D Model

In 2D it is not straight forward to establish a similar relation between the particle velocity and the constitutive relations. The constitutive relations give transport coefficients which are strongly dependent on the concentration. It is however still informative to consider the constant coefficient problem to get rough estimates of the influence of various parameters. The analysis of wall velocity needs special treatments since it appears only in the boundary conditions, see also Section **??**.

With η and $\tilde{D}$ constant the system of equations for $\boldsymbol{u}$ and p can be written as

$$\nabla \cdot (\tilde{D}\nabla p - \boldsymbol{u}) = 0 \tag{3.15}$$

$$\eta\Delta\boldsymbol{u} + (\eta + \lambda)\nabla\nabla \cdot \boldsymbol{u} - \nabla p = \boldsymbol{f}(\phi) \quad \text{in } \Omega \tag{3.16}$$

where $\Omega = \{(x, y) : 0 \leq x \leq H, 0 \leq y \leq H\}$.

$\boldsymbol{f}(\phi) = \Delta\rho\boldsymbol{g}\phi + \nabla p_s$, $\boldsymbol{u} = (u_1, u_2)$ are the velocity components in the x- and y-directions respectively and $\lambda = -2\eta/3$.

Boundary conditions are

$$u_1(0, y) = u_1(H, y) = 0 \quad u_1(x, 0) = u_{wall}(x) \quad u_{1,y}(x, H) = 0$$
$$u_2(x, 0) = u_2(x, H) = 0 \quad u_{2,x}(0, y) = u_{2,x}(H, y) = 0$$

Define the space $\boldsymbol{L}^2(\Omega)$ as

$$\boldsymbol{g} \in \boldsymbol{L}^2(\Omega) \text{ if } \int_\Omega |\boldsymbol{g}|^2 d\Omega < \infty$$

Also define the spaces $H^1(\Omega)$ and $\boldsymbol{H}^1(\Omega)$ as

$$\boldsymbol{g} = (g_1, g_2) \in \boldsymbol{H}^1(\Omega) \text{ if } g_i \in H^1(\Omega), \quad i = 1, 2$$

where a function g is in $H^1(\Omega)$ if the following holds

$$\int_\Omega (|g|^2 + |\nabla g|^2) d\Omega < \infty$$

We assume that there exists a solution p and $\boldsymbol{u}$ such that p is in $H^1(\Omega)$ and $\boldsymbol{u}$ is in $\boldsymbol{H}^1(\Omega)$. Also assume that $\boldsymbol{f}(\phi)$ is in $\boldsymbol{L}^2(\Omega)$. We require enough smoothness of $u_{wall}(x)$ that these assumptions will hold, see [21] and we obtain the estimate for $\boldsymbol{u}$

$$\|\boldsymbol{u}\|^2 \leq \frac{4}{(\eta C_\Omega)^2}\|\boldsymbol{f}\|^2 + \frac{2}{C_\Omega}\sum_i \|\nabla u_i^*\|^2 + \|\boldsymbol{u}^*\|^2. \tag{3.17}$$

which is proved below.

Here $\boldsymbol{u}^*$ is defined by $\boldsymbol{u} = \boldsymbol{u}^* + \hat{\boldsymbol{u}}$ where $\boldsymbol{u}^*$ satisfies $\nabla \cdot \boldsymbol{u}^*$ and the boundary conditions of $\boldsymbol{u}$ on $\partial\Omega$. Then $\hat{\boldsymbol{u}}$ satisfies homogeneous boundary conditions on $\partial\Omega$.

From the estimate given by equation (3.17) the velocity is bounded in terms of $1/\eta$, the bottom wall speed, u_{wall}, which is included in $\boldsymbol{u}^*$ and $\Delta\rho\boldsymbol{g}\phi$ which is included in $\boldsymbol{f}$.

However, we do not obtain any dependence on the permeability in the estimates, the direct relation between $\boldsymbol{u}$ and the consolidation speed which exists in 1D vanishes in 2D. Consider the time scale of concentration change

$$\frac{D\phi}{Dt} = -\phi \nabla \cdot \boldsymbol{u}$$

The consolidation rate is related to $q = \nabla \cdot \hat{\boldsymbol{u}}$. From (3.19) and (3.20) an equation for q follows,

$$\tilde{D}(2\eta + \lambda)\Delta q - q = \tilde{D}\nabla \cdot \boldsymbol{f}(\phi) \tag{3.18}$$

Unfortunately, q is not known on the boundary so (3.18) does not lead to estimates.

To prove the estimate (3.17) choose $\boldsymbol{u}^*$ such that $\boldsymbol{u}^* = (\psi_y, -\psi_x)$ then $\nabla \cdot \boldsymbol{u}^* = 0$. In order for $\boldsymbol{u}^*$ to satisfy the boundary conditions of $\boldsymbol{u}$ we should find a ψ such that

$$\psi_y(0,y) = \psi_y(H,y) = 0 \quad \psi_y(x,0) = u_{wall}(x) \quad \psi_{yy}(x,1) = 0$$
$$\psi_x(x,0) = \psi_x(x,1) = 0 \quad \psi_{xx}(0,y) = \psi_{xx}(1,y) = 0$$

ψ can be determined by e.g. transfinite interpolation [22] using fifth degree polynomials.

With $\boldsymbol{u} = \boldsymbol{u}^* + \hat{\boldsymbol{u}}$ and using the fact that $\nabla \cdot \boldsymbol{u}^* = 0$, (3.15) and (3.16) can be written as

$$\nabla \cdot (\tilde{D}\nabla p - \hat{\boldsymbol{u}}) = 0 \tag{3.19}$$
$$\eta\Delta(\boldsymbol{u}^* + \hat{\boldsymbol{u}}) + (\eta + \lambda)\nabla\nabla \cdot \hat{\boldsymbol{u}} - \nabla p = \boldsymbol{f}(\phi) \tag{3.20}$$

Multiply (3.19) with p, (3.20) with $\hat{\boldsymbol{u}}$ and use Green's formula to obtain

$$\int_\Omega (-\tilde{D}|\nabla p|^2 + \nabla p \cdot \hat{\boldsymbol{u}}) d\Omega = 0 \tag{3.21}$$

and

$$\int_\Omega (-\eta \sum_i \nabla \hat{u}_i \cdot \nabla(u_i^* + \hat{u}_i) - (\eta + \lambda)(\nabla \cdot \hat{\boldsymbol{u}}\nabla \cdot \hat{\boldsymbol{u}}) - \hat{\boldsymbol{u}} \cdot \nabla p)\partial\Omega =$$
$$\int_\Omega \boldsymbol{f} \cdot \hat{\boldsymbol{u}} d\Omega. \tag{3.22}$$

Add (3.21) and (3.22) to get

$$\int_\Omega (\tilde{D}|\nabla p|^2 + \eta \sum_i \nabla \hat{u}_i \cdot \nabla(u_i^* + \hat{u}_i) + (\eta + \lambda)\nabla \cdot \hat{\boldsymbol{u}}\nabla \cdot \hat{\boldsymbol{u}}) d\Omega = -\int_\Omega \boldsymbol{f} \cdot \hat{\boldsymbol{u}} d\Omega.$$

Introduce the usual L_2 norm, $\|\cdot\|$, defined by

$$\|f\|^2 = \int_\Omega |f|^2 d\Omega$$

then

$$\tilde{D}\|\nabla p\|^2 + \eta \sum_i \|\nabla \hat{u}_i\|^2 + (\eta + \lambda)\|\nabla \cdot \hat{\boldsymbol{u}}\|^2 \leq \|\boldsymbol{f}\|\|\hat{\boldsymbol{u}}\| + \eta \sum_i \|\nabla \hat{u}_i\|\|\nabla u_i^*\|.$$

It follows that

$$\eta \sum_i \|\nabla \hat{u}_i\|^2 \leq \|\boldsymbol{f}\|\|\hat{\boldsymbol{u}}\| + \eta \sum_i \|\nabla \hat{u}_i\|\|\nabla u_i^*\|.$$

By using the following inequality

$$\|g\|\|h\| \leq \frac{\sigma}{2}\|g\|^2 + \frac{1}{2\sigma}\|h\|^2 \tag{3.23}$$

we obtain

$$\frac{\eta}{2} \sum_i \|\nabla \hat{u}_i\|^2 \leq \|\boldsymbol{f}\|\|\hat{\boldsymbol{u}}\| + \frac{\eta}{2} \sum_i \|\nabla u_i^*\|^2. \tag{3.24}$$

Since $\hat{\boldsymbol{u}} \in \boldsymbol{H}_0^1$ e.i. $\hat{\boldsymbol{u}} \in \boldsymbol{H}^1$ and $\hat{\boldsymbol{u}} = 0$ on $\{(x, 0), \quad 0 \leq x \leq H\}$ we can use the Poincaré inequality, [21], and we have

$$\frac{\eta}{2} C_\Omega \|\hat{\boldsymbol{u}}\|^2 \leq \|\boldsymbol{f}\|\|\hat{\boldsymbol{u}}\| + \frac{\eta}{2} \sum_i \|\nabla u_i^*\|^2$$

where C_Ω is a constant depending only on H. Use the inequality (3.23) again yields

$$\|\hat{\boldsymbol{u}}\|^2 \leq \frac{4}{(\eta C_\Omega)^2}\|\boldsymbol{f}\|^2 + \frac{2}{C_\Omega} \sum_i \|\nabla u_i^*\|^2. \tag{3.25}$$

and (3.17) follows.

An estimate for the space derivative of $\boldsymbol{u}$ can be obtained using (3.24) and (3.25) as

$$\sum_i \|\nabla u_i\|^2 \leq \frac{4}{\eta^2 C_\omega}\|\boldsymbol{f}\|^2 + \sum_i \|\nabla u_i^*\|^2 \tag{3.26}$$

Chapter 4

Numerical Methods

In this section we discuss numerical methods and algorithms used to design a solver for a one- and two dimensional consolidation problem. The equations are discretized using finite difference methods both in space and time. The solver is written using MATLAB® [17].

The mathematical models are given by equations (3.4)-(3.6) in the one dimensional case and by (3.1) - (3.3) in the two dimensional case.

4.1 Finite Differences

To approximate the equations numerically we use the method of finite differences. Standard finite difference methods require a rectangular grid with equally spaced grid points. To be able to use a non-uniform grid, for example using more grid-points near a boundary, the numerical code is implemented in such a way that it automatically transforms the equations from the physical (x, y)-domain, which in some sense can be arbitrary, to a generalized curvilinear (r, s)-space, [11]. The equations will be expressed in terms of the generalized coordinates and discretized on a rectangular computational domain with a uniform grid, see figure (4.1).

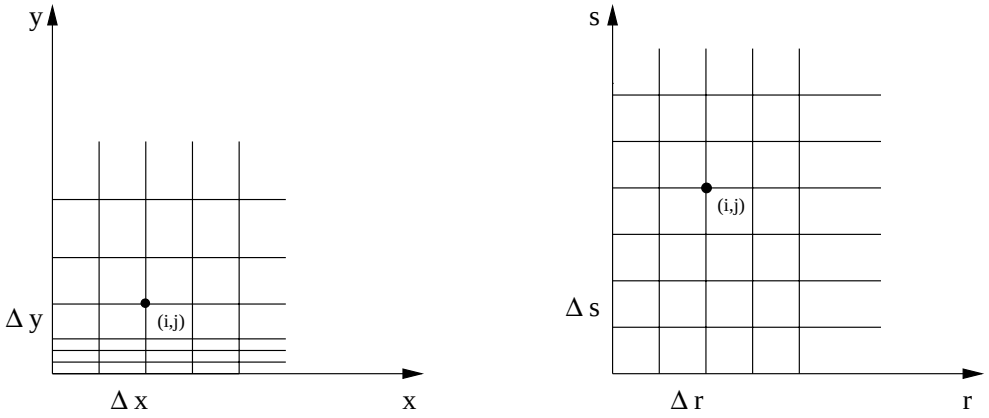

Figure 4.1. Physical domain transformed to a computational domain

Let the computational domain be described by the coordinates (r, s) and the physical domain by (x, y). The independent variables in the physical space, (x, y) are transformed to the variables in the computational space, (r, s) by

$$r = r(x, y), \quad s = s(x, y)$$

The transformation has to be smooth and a point in the physical space must correspond to one and only one point in the computational domain. To express the equation in the computational domain we need to transform the derivatives by the chain rule. Higher order derivatives are implemented as repeated first derivatives, so only first order mapping derivatives, the elements of the Jacobian, or the metrics, appear in the transformed equations.

The metrics are evaluated numerically using second order central schemes. In what follows, we describe the difference operators for a uniform grid .

Introduce the following grid functions for the unknowns:

$$\phi_{i,j} = \phi(x_i, y_j) \qquad p_{i,j} = p(x_i, y_j)$$

$$u_{i,j} = u(x_i, y_j) \qquad v_{i,j} = v(x_i, y_j)$$

We use the notation

Forward difference, first order accurate:

$$D_+^x u_{i,j} = \frac{u_{i+1,j} - u_{i,j}}{\Delta x_i} = (u_x)_{i,j} + \mathcal{O}(\Delta x)$$

Backward difference, first order accurate:

$$D_-^x u_{i,j} = \frac{u_{i,j} - u_{i-1,j}}{\Delta x_i} = (u_x)_{i,j} + \mathcal{O}(\Delta x)$$

Central difference, second order accurate:

$$D_0^x u_{i,j} = \frac{u_{i+1,j} - u_{i-1,j}}{2\Delta x_i} = (u_x)_{i,j} + \mathcal{O}((\Delta x)^2)$$

Second order derivatives are implemented with second order accurate schemes

$$D_+^x D_-^x u_{i,j} = \frac{u_{i+1,j} - 2u_{i,j} + u_{i-1,j}}{(\Delta x_i)^2} = (u_{xx})_{i,j} + \mathcal{O}((\Delta x)^2)$$

4.2 Numerical Treatment of the 1D Model

As a model of a 1D problem, let the suspension be confined in a closed box of height H. The particles will consolidate due to the gravity force pointing in the negative y-direction, see Figure 4.2.

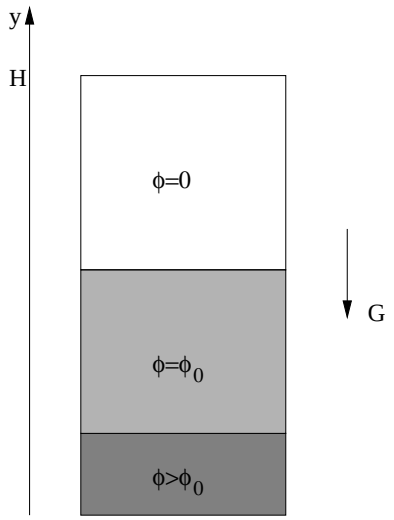

Figure 4.2. Setup for the consolidation process in a closed container. The suspension consolidates only due to gravity and the process can be considered as one dimensional.

The governing equations in this case are given by

$$\frac{\partial \phi}{\partial t} + \frac{\partial (v\phi)}{\partial y} = 0 \tag{4.1}$$

$$\frac{\partial}{\partial y}\left(\tilde{D}\frac{\partial p}{\partial y}\right) - \frac{\partial v}{\partial y} = 0 \tag{4.2}$$

$$\frac{4}{3}\frac{\partial}{\partial y}(\eta\frac{\partial v}{\partial y}) - \frac{\partial p}{\partial y} = \frac{\partial p_s}{\partial y} + \phi g(\rho_s - \rho_f) \tag{4.3}$$

where $\tilde{D} = D(\phi)(1-\phi)$, p_s and η are given functions of ϕ.

The container is assumed to be closed and the walls to be impermeable which motivates the use of the following boundary conditions

$$v(0) = v(H) = 0 \tag{4.4}$$

$$\frac{\partial p}{\partial y}(0) = \frac{\partial p}{\partial y}(H) = 0 \tag{4.5}$$

In Section 4.2.1 we consider two different ways of discretizing (4.2)-(4.3), central differences with artificial viscosity and a scheme where the convective terms are approximated with one-sided differences. Since the pressure is determined only "up to a constant" by these equations and the Neumann boundary condition, the pressure equation needs special treatment, see Section 4.2.2 and Section 4.2.3.

The continuity equations is treated by an upwind scheme, see Section 4.2.4.

Let the y-t plane be discretized with a constant mesh size h and a time step k and let

$$\begin{aligned} y_j &= (j-1)h, \quad j = 1, ...N \\ t_n &= nk, \qquad\quad n = 0, 1, ... \end{aligned}$$

Since there is only one independent space variable, y, the superscript on the differences are excluded since they all denote approximations of space derivatives with respect to y.

4.2.1 Discretization of the Elliptic System

Using central difference to approximate both the diffusive and the convective terms yields,

$$\frac{4}{3} D_+ \left(\eta_{j-\frac{1}{2}} D_- v_j \right) - D_0 p_j = D_+ p_s(\phi_j) + \phi_j g(\rho_s - \rho_f) \tag{4.6}$$

$$D_- \left(\tilde{D}_{j+\frac{1}{2}} D_+ p_j \right) - D_0 v_j = 0. \tag{4.7}$$

where $\eta_{j-\frac{1}{2}}$ is computed as the mean value $\frac{\eta_{j-1}+\eta_j}{2}$. Similar with $\tilde{D}_{j+\frac{1}{2}}$.

This scheme imposes a severe restriction on the mesh size to avoid oscillations, similar to the cell Peclet number limit for central difference schemes for the convection-diffusion equation.

This can be explained by looking at the homogeneous system of difference equations for the approximate solution, assuming η and $\tilde{D}$ are constants.

$$\frac{\eta}{h^2}(v_{j+1} - 2v_j + v_{j-1}) - \frac{1}{2h}(p_{j+1} - p_{j-1}) = 0$$

$$-\frac{1}{2h}(v_{j+1} - v_{j-1}) + \frac{\tilde{D}}{h^2}(p_{j+1} - 2p_j + p_{j-1}) = 0$$

The anzats

$$u_j = U\lambda^j, \quad v_j = V\lambda^j,$$

yields the eigenvalue problem for λ

$$\begin{pmatrix} \frac{\eta}{h^2}(\lambda^2 - 2\lambda + 1) & -\frac{1}{2h}(\lambda^2 - 1) \\ -\frac{1}{2h}(\lambda^2 - 1) & \frac{\tilde{D}}{h^2}(\lambda^2 - 2\lambda + 1) \end{pmatrix} \begin{pmatrix} V_j \\ P_j \end{pmatrix} = \begin{pmatrix} 0 \\ 0 \end{pmatrix}.$$

Non-oscillative solutions are guaranteed by λ real and positive, which requires

$$h \leq 2\sqrt{\eta \tilde{D}} \tag{4.8}$$

$\sqrt{\eta \tilde{D}}$, the square root of the "apparent permeability" is also related to the size of the boundary layer which appears in the velocity profile due to the viscous terms in the equations, typically for the material studied $0.1 - 1mm$. The size of the computational domain is of order 0.1 m, and a uniform grid satisfying (4.8) is too costly.

The standard recipe to avoid oscillations is to artificially increase the amount of viscosity. For a given step size h the total viscosity, $\hat{\eta}$, should be large enough to fulfill the restriction given by equation (4.8). In this case the viscosity could be modified as

$$\hat{\eta} = \max(\frac{h^2}{4\tilde{D}}, \eta) \tag{4.9}$$

Another way of avoiding oscillatory solutions is to discretize the convective terms in (4.6) and (4.7) by first order differences chosen properly.

$$\frac{4}{3} D_+ \left(\eta_{j-\frac{1}{2}} D_- v_j \right) - D_+ p_j = D_+ p_s(\phi_j) + \phi_j g(\rho_s - \rho_f) \tag{4.10}$$

$$D_- \left(\tilde{D}_{j+\frac{1}{2}} D_+ p_j \right) - D_- v_j = 0 \tag{4.11}$$

If $\delta = h^2/\eta\tilde{D}$ then, following the procedure above, λ will be positive and real if

$$2 + \delta > \sqrt{(2+\delta)^2 - 4}$$

which is true for all $\delta > 0$.

There is no restriction at all on the step size, and the approximate solution in this case is never oscillatory.

One can show that to first order, the upstream-downstream scheme for the 1D problem is equivalent to taking $\tilde{\eta} = \eta + h^2/4\tilde{D}$.

4.2.2 Pressure Non-Unicity Problem

The equations (4.2) and (4.3) depend only on p through its derivatives. Since the boundary conditions are given as the normal derivative of p, a solution to this problem will not be uniquely determined. If $p(y)$ is a solution, then for any constant C the function $p_C = p(y) + C$ is also a solution. This will cause some difficulties in the numerical solution that are considered below, [19].

The discrete version of the elliptic equations can be written as a linear system of equation for the $2N$ unknowns gathered in the vectors $\boldsymbol{v}, \boldsymbol{p} \in \mathbb{R}^N$.

$$\underbrace{\begin{pmatrix} L_{11} & L_{12} \\ L_{21} & L_{22} \end{pmatrix}}_{L} \begin{pmatrix} \boldsymbol{v} \\ \boldsymbol{p} \end{pmatrix} = \begin{pmatrix} \boldsymbol{f} \\ 0 \end{pmatrix} \tag{4.12}$$

L_{11} and $L_{22} \in \mathbb{R}^{N\times N}$ and represent the discrete second order derivative operator applied to $\boldsymbol{v}$ and $\boldsymbol{p}$. $L_{12}, L_{21} \in \mathbb{R}^{N\times N}$ represent the first order derivative operators on $\boldsymbol{v}$ and $\boldsymbol{p}$ respectively. $\boldsymbol{f} \in \mathbb{R}^N$ is given by the right hand side of (4.10).

The non-uniqueness of the pressure solution implies that the matrix L is singular.:

$$\begin{pmatrix} L_{11} & L_{12} \\ L_{21} & L_{22} \end{pmatrix} \begin{pmatrix} 0 \\ \alpha \boldsymbol{p}_0 \end{pmatrix} = 0 \tag{4.13}$$

where $\alpha\boldsymbol{p}_0$ is the vector spanning the right null space of L_{22}, a vector of all ones.

To obtain a unique pressure solution an additional condition or constraint on the system is required.

There is also a single vector $\boldsymbol{n}$ such that $\boldsymbol{n}^T L_{22} = 0$. If L_{22} is symmetric, $\boldsymbol{n} = \alpha\boldsymbol{p}_0$.

If we multiply the last equation in (4.12) from the left with $\boldsymbol{n}^T$ we get

$$\boldsymbol{n}^T L_{21} \boldsymbol{v} = 0 \tag{4.14}$$

where we have used $\boldsymbol{n}^T L_{22} = 0$.

Equation (4.14) represents the condition that has to be satisfied in order to have any solutions to (4.12). Depending on the implementation of boundary conditions and due to round off errors, equation (4.14) is in general not satisfied exactly and there are no solutions to (4.12). In that case, instead of solving $L_{21}\boldsymbol{v} + L_{22}\boldsymbol{p} = 0$ the following constrained minimization problem is solved

$$\min_{\boldsymbol{m}^T\boldsymbol{p}=0} \|L_{22}\boldsymbol{p} + L_{21}\boldsymbol{v}\|_2.$$

Where the constraint $\boldsymbol{m}^T\boldsymbol{p} = 0$ is added in order to get a unique solution. $\boldsymbol{m}$ could be arbitrary as long as $\boldsymbol{m}^T\boldsymbol{p}_0$ is non-zero, and we will take $\boldsymbol{m} = \boldsymbol{p}_0$ in the theorem below. That a unique solution exists to the minimization problem is shown by the following theorem:

Theorem 4.1. *Assume that* $\dim(null(L_{22})) = 1$ *and* $\boldsymbol{n}^T L_{22} = 0$. *Then the solution of* $\min \|L_{22}\boldsymbol{p} - \boldsymbol{b}\|_2$ *s.t.* $\boldsymbol{p}_0^T\boldsymbol{p} = 0$ *is unique and given by*

$$\begin{pmatrix} L_{22} & \boldsymbol{n} \\ \boldsymbol{p}_0^T & 0 \end{pmatrix} \begin{pmatrix} \boldsymbol{p} \\ \beta \end{pmatrix} = \begin{pmatrix} \boldsymbol{b} \\ 0 \end{pmatrix} \tag{4.15}$$

Proof. Define a residual as $\boldsymbol{r} = L_{22}\boldsymbol{p} - \boldsymbol{b}$ then in order to find $\min \|L_{22}\boldsymbol{p} - \boldsymbol{b}\|_2$, $L_{22}^T\boldsymbol{r} = 0$ or equally $\boldsymbol{r}^T L_{22} = 0$. Compared with the fact that $\boldsymbol{n}^T L_{22} = 0$ and that $dim(null(L_{22})) = 1$ the residual can be written as $\boldsymbol{r} = -\beta\boldsymbol{n}$. β is a constant to be determined and the solution to the minimization problem is given by equation (4.15)

The solution is unique if the only solution to the homogeneous problem

$$\begin{pmatrix} L_{22} & \boldsymbol{n} \\ \boldsymbol{p}_0^T & 0 \end{pmatrix} \begin{pmatrix} \boldsymbol{y} \\ \kappa \end{pmatrix} = 0 \tag{4.16}$$

is $\begin{pmatrix} \boldsymbol{y} \\ \kappa \end{pmatrix} = 0$

Multiply the first equation in (4.16) with $\boldsymbol{n}^T$ from the left and use the fact that $\boldsymbol{n}^T L_{22} = 0$, then

$$\boldsymbol{n}^T\boldsymbol{n}\kappa = 0, \qquad \Rightarrow \kappa = 0$$

This together with the second equation yields

$$L_{22}\boldsymbol{y} = 0 \quad \text{and} \quad \boldsymbol{p}_0^T\boldsymbol{y} = 0$$

Using the fact that $L_{22}\alpha\boldsymbol{p}_0 = 0$ and since $\alpha\boldsymbol{p}_0^T\boldsymbol{p}_0 \neq 0$ then $\boldsymbol{y} = 0$. Hence the solution is unique.

So, instead of solving (4.12)

$$\begin{aligned} L_{11}\boldsymbol{v} + L_{12}\boldsymbol{p} &= \boldsymbol{f} \\ L_{21}\boldsymbol{v} + L_{22}\boldsymbol{p} + \beta\boldsymbol{n} &= 0 \\ \boldsymbol{p}_0^T\boldsymbol{p} &= 0 \end{aligned} \tag{4.17}$$

are solved.

4.2.3 Implementation of Boundary Conditions

The pressure boundary conditions are implemented as follows:

$$\begin{aligned} \frac{\partial p}{\partial y}(0) &= -\frac{p_1 - p_2}{\Delta y} = 0 \\ \frac{\partial p}{\partial y}(H) &= -\frac{p_N - p_{N-1}}{\Delta y} = 0 \end{aligned} \tag{4.18}$$

where we use a first order stencil in order to preserve the symmetry of the discrete operator, L_{22}.

The size of the correction term, $\beta\boldsymbol{n}$, introduced in the previous section, depends on the choice of discretization of the equations as well as the the velocity boundary conditions.

β can be determined by multiply the last equation in (4.17) from the left with $\boldsymbol{n}^T$

$$\boldsymbol{n}^T L_{22}\boldsymbol{p} + \boldsymbol{n}^T L_{21}\boldsymbol{v} = -\boldsymbol{n}^T\beta\boldsymbol{n}, \Rightarrow \beta = -\frac{\boldsymbol{n}^T L_{21}\boldsymbol{v}}{\boldsymbol{n}^T\boldsymbol{n}}$$

and we see that if (4.14) is true then β is equal to zero and $L_{22}\boldsymbol{p} + L_{21}\boldsymbol{v} = 0$. So, in order to get the correction term as small as possible we would like to have β as close to zero as possible.

The left null vector of L_{22} will be a constant vector, $\boldsymbol{n}^T = \gamma(1, 1, \cdots, 1)$ with $\boldsymbol{n}^T\boldsymbol{n} = 1$. When one-sided differences are used to approximate the convective terms, the size of β can be computed as

$$\beta = -\gamma \sum_{j=1}^{j=N} D_- v_j = \frac{\gamma}{h} v_2$$

In this case it is difficult to choose the implementation of the boundary conditions in such a way that β is minimized. If instead a central difference is used

$$\beta = -\gamma \sum_{j=1}^{j=N} D_0 v_j = \frac{\gamma}{2h}(v_1 + v_2 - (v_N + v_{N-1}))$$

and if boundary conditions for the velocity are approximated as

$$v(0) = \frac{v_1 + v_2}{2} = 0 \tag{4.19}$$
$$v(H) = \frac{v_N + v_{N-1}}{2} = 0$$

β will be equal to zero as well as the correction term, $\beta \boldsymbol{n}$.

To conclude, a central second order scheme should be used to approximate the convective terms with boundary conditions implemented as (4.19). This in order to minimize the effect of the pressure correction. However, the viscosity has to be modified in order to obtain solutions free from oscillations.

In Section 5.2 we report a convergence study of the scheme and we show that β in fact is a small number in the computations.

4.2.4 Numerical Treatment of the Conservation Equation for ϕ

Since we know that the solution to the hyperbolic equation, (4.1), can develop discontinuous solutions, a conservative upwind method should be used to prevent oscillations in the vicinity of discontinuities. Since the equation is nonlinear and the sign of the characteristic speed may change during the computation, a simple one-sided difference method cannot be used. Instead ideas from Godunov's method [16] are used.

Write equation (4.1) as

$$\phi_t + f(\phi, v(y;\phi))_y = 0 \tag{4.20}$$

where $f(\phi, v(y;\phi)) = \phi v(y;\phi)$. The notation $v(y;\phi)$ indicates that v is obtained as the solution of the elliptic system (4.2) - (4.3), where the source term and the coefficients are functions of ϕ.

Approximate (4.20) by

$$\frac{\phi_j^{n+1} - \phi_j^n}{k} + \frac{\tilde{f}_{j+1/2}^n - \tilde{f}_{j-1/2}^n}{h} = 0 \tag{4.21}$$

where $\tilde{f}_{j+1/2} = f(\phi_j, \phi_{j+1}, v_j, v_{j+1})$ and is called the numerical flux function. The numerical flux is defined depending on the sign of the characteristic speed. This is given by differentiating the flux function with respect to ϕ.

$$f' = f_\phi = v + \phi v_\phi \tag{4.22}$$

To define $\tilde{f}$ the following cases have to be considered, see Figure 4.3. How the different terms are approximated numerically is explained below.

1. **if** $f'_R < f'_L$ **and** $s_{j+1/2} > 0$ (shock moving to the right)
   then $\tilde{f}_{j+1/2} = f(\phi_j, v_j)$
2. **if** $f'_R < f'_L$ **and** $s_{j+1/2} < 0$ (shock moving to the left)
   then $\tilde{f}_{j+1/2} = f(\phi_{j+1}, v_{j+1})$

3. **if** $f'_R \geq f'_L$ **and** $f'_L \geq 0$ **then** $\tilde{f}_{j+1/2} = f(\phi_j, v_j)$

4. **if** $f'_R \geq f'_L$ **and** $f'_R < 0$ **then** $\tilde{f}_{j+1/2} = f(\phi_{j+1}, v_{j+1})$

5. **if** $f'_R > 0$ **and** $f'_L < 0$ **then** $\tilde{f}_{j+1/2} = f(\phi^*, v^*)$

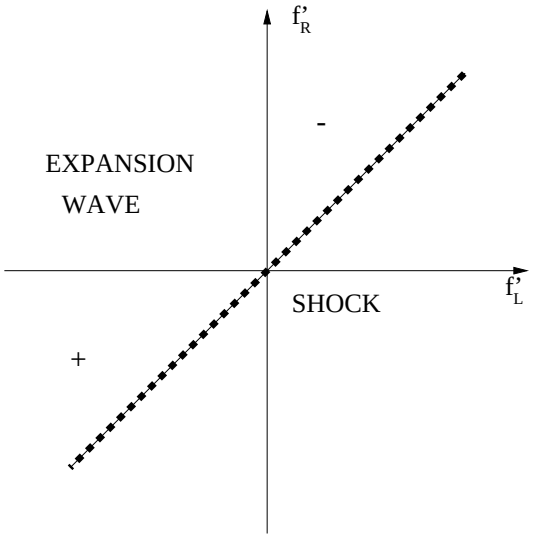

Figure 4.3. The different cases considered in the Godunov scheme. All conditions under the dashed line are characterized by a shock solution. The minus sign corresponds to case 3 where the characteristics are diverging with a negative slope. The plus sign corresponds to case 4 where they are diverging but with a positive slope. Finally the expansion wave area corresponds to case 5.

Since v does not explicitly depend on ϕ, f' can only be evaluated numerically, using the following approximation, see Figure 4.4 below:

$$f'_L \approx v_j + \phi_j \frac{\Delta\phi_j \Delta v_j}{\Delta\phi_j^2 + \varepsilon} \tag{4.23}$$

and

$$f'_R \approx v_{j+1} + \phi_{j+1} \frac{\Delta\phi_j \Delta v_j}{\Delta\phi_j^2 + \varepsilon} \tag{4.24}$$

where ε is a small number and where

$$\Delta v_j = v_{j+1} - v_j \quad \Delta\phi_j = \phi_{j+1} - \phi_j \tag{4.25}$$

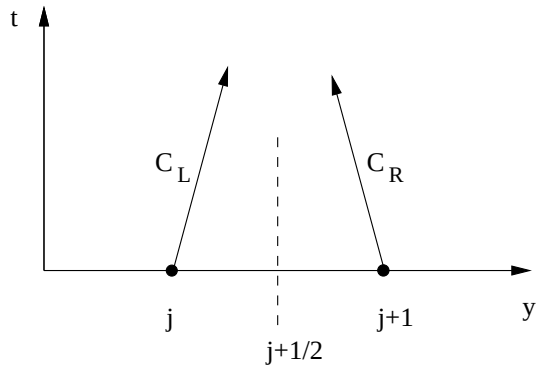

Figure 4.4. The slope of the characteristic on the left side of the cell interface $y_{j+1/2}$, C_L is given by $1/f'_L$ and the slope of C_R is given by $1/f'_R$

$\frac{\Delta v_j}{\Delta \phi_j}$ is replaced by $\frac{\Delta \phi_j \Delta v_j}{\Delta \phi_j^2 + \varepsilon}$ to avoid dividing by zero when ϕ is constant.
s denotes the shock speed defined by

$$s = \frac{[f]}{[\phi]} \tag{4.26}$$

where $[\cdot]$ denotes the jump across the discontinuity. In the difference scheme the shock speed is approximated as

$$s_{j+1/2} = \frac{\Delta \phi_j \Delta f_j}{\Delta \phi_j^2 + \varepsilon} \tag{4.27}$$

where $\Delta f_j = \phi_{j+1} v_{j+1} - \phi_j v_j$.

In case 5 the characteristics form a transsonic expansion wave, see Figure 4.5 and (ϕ^*, v^*) should be chosen such that $f'(\phi^*, v^*) = 0$.

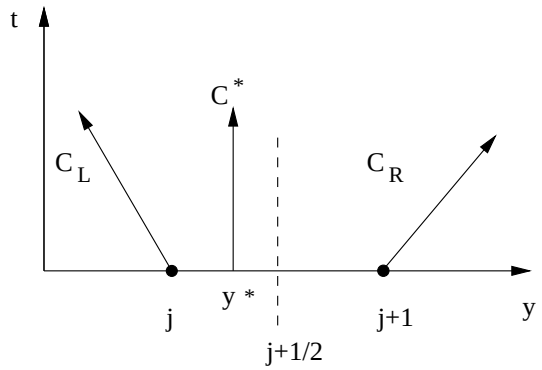

Figure 4.5. Transsonic expansion wave. C^* is the characteristic given by $f'(\phi^*, v(y^*; \phi^*)) = 0$.

To find ϕ^* and $v^* \in [y_j, y_{j+1}]$ such that $f' = 0$, assume that ϕ and v are linear functions of $y \in [y_j, y_{j+1}]$. Then they can be written as

$$v(y) = v_j + \alpha(v_{j+1} - v_j), \quad \phi(y) = \phi_j + \alpha(\phi_{j+1} - \phi_j)$$

where $\alpha = (y - y_j)/h$.

Then using equation (4.22) we obtain

$$v_j + \alpha(v_{j+1} - v_j) + (\phi_j + \alpha(\phi_{j+1} - \phi_j))\frac{\Delta v_j}{\Delta \phi_j} = 0$$

from this α can be determined as

$$\alpha = -\frac{1}{2}\left(\frac{v_j}{\Delta v_j} + \frac{\phi_j}{\Delta \phi_j}\right)$$

and

$$f(\phi^*, v^*) = \frac{1}{2}\phi_j v_j - \frac{1}{4}\left(v_j^2 \frac{\Delta \phi_j}{\Delta v_j} + \phi_j^2 \frac{\Delta \phi_j \Delta v_j}{\Delta \phi_j^2 + \varepsilon}\right)$$

4.2.5 Numerical Algorithm

The hyperbolic equation and the elliptic system are coupled through the velocity field, v and the volume fraction ϕ. To compute ϕ^{n+1} we use the velocity at $t = t^n$, v^n. And to compute the velocity and the pressure at $t = t^n$, we let the coefficients and the forcing function in the elliptic system depend on ϕ^n. If ϕ^n is known at time $t = t^n$

- Compute $\eta^n = \eta(\phi^n)$, $p_s^n = p_s(\phi^n)$ and $\tilde{D}^n = (\phi^n)$
- Construct the discrete elliptic operator, L and (if necessary) compute the left null vector of L_{22}. Of course, when the discretization of the equations and the boundary conditions are properly chosen $\boldsymbol{n}$ may be known. For the general case, the vector $\boldsymbol{n}^T$ is determined by the relation $\boldsymbol{n}^T L_{22} = 0$. Finding the left eigenvector corresponding to the zero eigenvalue of L_{22} can efficiently be done by the shifted inverse power method

  $$\boldsymbol{n}^{k+1} = (L_{22}^T - \varepsilon I)^{-1}\boldsymbol{n}^k, \quad \boldsymbol{n}^{k+1} = \frac{\boldsymbol{n}^{k+1}}{\|\boldsymbol{n}^{k+1}\|_2} \tag{4.28}$$

  where ε is a small positive number. Only a few iterations are needed in order for the algorithm to converge.

- Solve an extended linear system of equations of size $(2N + 1) \times (2N + 1)$. This is given by the discretization of the elliptic system and the minimization process discussed in Section 4.2.2, $L(\eta^n, \tilde{D}^n)\boldsymbol{w}^n = F(p_s^n, \phi^n)$, for $\boldsymbol{w} = (\boldsymbol{v},\ \boldsymbol{p},\ -\beta)$.

  L is a sparse matrix and a direct method for sparse systems is used to solve $L\boldsymbol{w} = F$.

- Finally, solve for ϕ^{n+1} by using the Godunov's scheme described in Section 4.2.4.

The time step is chosen to fulfill the CFL-condition. As initial condition we use a given profile for ϕ.

4.3 Numerical Treatment of the 2D Model

Two dimensional effects of shear are studied with the suspension in a box with moving bottom wall. The gravity is directed in the negative y-direction, see figure (4.6).

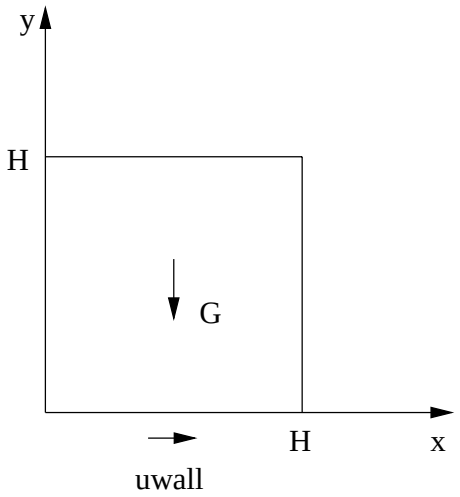

Figure 4.6. Setup for studying the consolidation process. Closed container with a bottom wall which in the 2D case is moving with a velocity uwall

The set of equations, (3.1) - (3.3), yields four equations for the unknowns; p, $\boldsymbol{u} = (u, v)$ and ϕ. u and v are the components of the particle velocity in x and y-direction respectively. Together with the constitutive relation for $\boldsymbol{\tau}_s$ given by (2.10) the following system of partial differential equations is obtained

$$\frac{\partial \phi}{\partial t} + \frac{\partial (u\phi)}{\partial x} + \frac{\partial (v\phi)}{\partial y} = 0 \tag{4.29}$$

$$\frac{\partial}{\partial x}\left(\tilde{D}\frac{\partial p}{\partial x}\right) + \frac{\partial}{\partial y}\left(\tilde{D}\frac{\partial p}{\partial y}\right) - \frac{\partial u}{\partial x} - \frac{\partial v}{\partial y} = 0 \tag{4.30}$$

$$\begin{aligned}\frac{4}{3}\frac{\partial}{\partial x}\left(\eta\frac{\partial u}{\partial x}\right) - \frac{2}{3}\frac{\partial}{\partial x}\left(\eta\frac{\partial v}{\partial y}\right) + \frac{\partial}{\partial y}\left(\eta\frac{\partial u}{\partial y}\right) + \frac{\partial}{\partial y}\left(\eta\frac{\partial v}{\partial x}\right) \\ - \frac{\partial p}{\partial x} = \frac{\partial p_s}{\partial x}\end{aligned} \tag{4.31}$$

$$\begin{aligned}\frac{4}{3}\frac{\partial}{\partial y}\left(\eta\frac{\partial v}{\partial y}\right) - \frac{2}{3}\frac{\partial}{\partial y}\left(\eta\frac{\partial u}{\partial x}\right) + \frac{\partial}{\partial x}\left(\eta\frac{\partial v}{\partial x}\right) + \frac{\partial}{\partial x}\left(\eta\frac{\partial u}{\partial y}\right) \\ - \frac{\partial p}{\partial y} = \frac{\partial p_s}{\partial y} + \phi(\rho_s - \rho_f)g\end{aligned} \tag{4.32}$$

where $\tilde{D} = D(\phi)(1-\phi)$, $\eta = \eta(\phi, \dot{\gamma})$ and $p_s = p_s(\phi, \phi^*)$.

Boundary conditions have to be specified for the velocity components and the pressure on all boundaries.

We assume that the friction between the bottom wall and the particles is large and a non-slip condition is imposed. On the side walls and on the top we assume no friction and slip conditions are used. The normal velocity is equal to zero on all boundaries.

$$u(0,y) = u(H,y) = 0 \quad u(x,0) = u_{wall}, \quad \frac{\partial u}{\partial y}(x,H) = 0$$

$$v(x,0) = v(x,H) = 0, \quad \frac{\partial v}{\partial x}(0,y) = \frac{\partial v}{\partial x}(H,y) = 0$$

The impermeable walls are consistent with the boundary condition for the reduced pressure

$$\frac{\partial p}{\partial n} = 0$$

on all boundaries.

We discretize in space by a tensor product, non-uniform rectangular grid (x_i, y_j), $i, j = 1, \cdots, N_x, N_y$ where N_x, N_y are the number of grid points in each direction.

4.3.1 Discretization of the Elliptic System

As in the one dimensional case, see Section 4.2.1 we choose to use central differences for the convective terms and artificially add viscosity to avoid oscillations in the solution. The viscosity is modified according to

$$\eta^x_{i,j} = \max\left(c^x_\eta \frac{\Delta x_i^2}{4\tilde{D}(\phi_{i,j})}, \eta(\phi_{i,j}, |\dot{\gamma}|_{i,j})\right) \quad \eta^y_{i,j} = \max\left(c^y_\eta \frac{\Delta y_j^2}{4\tilde{D}(\phi_{i,j})}, \eta(\phi_{i,j}, |\dot{\gamma}|_{i,j})\right)$$

where c^x_η and c^y_η are constants to be chosen less than one. Using the notation introduced in Section 4.1 equations (4.30), (4.31) and (4.32) can be written in their discrete form as

$$D^x_+(\tilde{D}_{i-\frac{1}{2},j} D^x_- p_{i,j}) + D^y_+(\tilde{D}_{i,j-\frac{1}{2}} D^y_- p_{i,j}) - D^x_0 u_{i,j} - D^y_0 v_{i,j} = 0 \tag{4.33}$$

And for the two components of the momentum equation we obtain

$$\begin{aligned} \frac{4}{3} D^x_+(\eta^x_{i-\frac{1}{2},j} D^x_- u_{i,j}) - \frac{2}{3} D^x_0(\eta_{i,j} D^y_0 v_{i,j}) + D^y_+(\eta_{i,j-\frac{1}{2}} D^y_- u_{i,j}) + \\ D^y_0(\eta_{i,j} D^x_0 v_{i,j}) - D^x_0 p_{i,j} = D^x_+ p_{si,j} \end{aligned} \tag{4.34}$$

and

$$\begin{aligned} \frac{4}{3} D^y_+(\eta^y_{i,j-\frac{1}{2}} D^y_- v_{i,j}) - \frac{2}{3} D^y_0(\eta_{i,j} D^x_0 u_{i,j}) + D^x_+(\eta_{i-\frac{1}{2},j} D^x_- v_{i,j}) + \\ D^x_0(\eta_{i,j} D^y_0 u_{i,j}) - D^y_0 p_{i,j} = D^y_+ p_{si,j} + g(\rho_s - \rho_f)\phi_{i,j} \end{aligned} \tag{4.35}$$

The boundary conditions are implemented to minimize the effect of the pressure correction, see Section 4.2.3,

$$u(0,y) = \frac{1}{2}(u_{1,j} + u_{2,j}) = 0 \quad u(H,y) = \frac{1}{2}(u_{N_x,j} + u_{N_x-1,j}) = 0 \tag{4.36}$$

and

$$v(x,0) = \frac{1}{2}(v_{i,1} + v_{i,2}) = 0 \quad v(x,H) = \frac{1}{2}(v_{i,N_y} + u_{i,N_y-1}) = 0 \tag{4.37}$$

To avoid inconsistency in the velocity boundary conditions in the lower right and left corner we let the velocity of the bottom wall go gradually to zero at the vertical walls over a few points.

The boundary condition for the reduced pressure is implemented as

$$\frac{\partial p}{\partial x}(0,y) = -\frac{p_{1,j} - p_{2,j}}{\Delta x_1} \tag{4.38}$$

and similar for the other boundaries and the slip conditions on the velocities. By using a mesh according to Figure 4.7 we obtain second order accurate approximations of the boundary conditions.

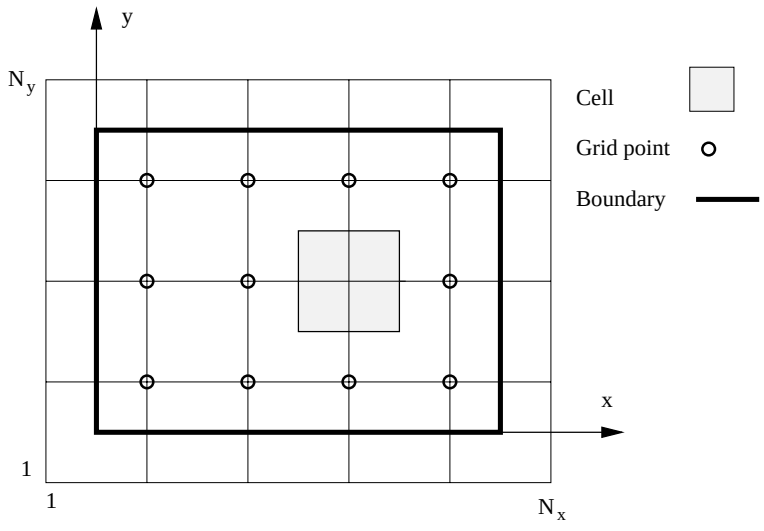

Figure 4.7. The mesh used in the computations.

The pressure solution is taken care of in the same way as described in Section 4.2.2 and the discretization of the elliptic system produces the following linear system of equations to be solved for the unknowns $\boldsymbol{p}$, $\boldsymbol{u}$ and $\boldsymbol{v}$.

$$\underbrace{\begin{pmatrix} M_{11} & M_{12} & 0 \\ M_{21} & M_{22} & \boldsymbol{n} \\ 0 & \boldsymbol{n}^T & 0 \end{pmatrix}}_{M} \begin{pmatrix} \boldsymbol{w} \\ \boldsymbol{p} \\ \beta \end{pmatrix} = \begin{pmatrix} \boldsymbol{F} \\ 0 \\ 0 \end{pmatrix} \tag{4.39}$$

where $M \in \mathbb{R}^{3NxNy+1 \times 3NxNy+1}$, $(\boldsymbol{w} \;\; \boldsymbol{p})^T \in \mathbb{R}^{3NxNy}$ contains the values of the unknowns on the grid including the boundary points and $\boldsymbol{w} = (\boldsymbol{u} \; \boldsymbol{v})^T$. $(\boldsymbol{F} \;\; 0)^T \in \mathbb{R}^{3NxNy}$ contains the values of the right hand sides of the discrete version of the equations. $\boldsymbol{n}$ is the null vector of M_{22}^T, the discrete elliptic operator applied to p from equation (4.33). If the null vector needs to be computed, we use the shifted inverse power method according to algorithm (4.28).

4.3.2 Conservation Equation for ϕ

To solve

$$\phi_t + f(\phi, u(x, y; \phi))_x + g(\phi, v(x, y; \phi))_y = 0 \tag{4.40}$$

where

$$f(\phi, u(x, y; \phi)) = \phi u(x, y; \phi), \qquad g(\phi, v(x, y; \phi)) = \phi v(x, y; \phi) \tag{4.41}$$

we extend the upwind scheme treated in Section 4.2.4 to the multi-dimensional problem. This is done by treating the cell face fluxes one-dimensionally. For each cell two Riemann problems are solved, one in the x-direction associated with the flux component f, and one in the y-direction associated with g. This leads to the following scheme

$$\phi_{i,j}^{n+1} = \phi_{i,j}^n - \frac{k}{\Delta x_i}(\tilde{f}_{i+1/2,j} - \tilde{f}_{i-1/2,j}) - \frac{k}{\Delta y_j}(\tilde{g}_{i,j+1/2} - \tilde{g}_{i,j-1/2})$$

where $\tilde{f}$ and $\tilde{g}$ are the numerical flux functions. They are, as described in Section 4.2.4, defined depending on the sign of the characteristic speeds given by differentiating the flux functions with respect to ϕ

$$f' = f_\phi = u + \phi u_\phi \quad g' = g_\phi = v + \phi v_\phi$$

Numerically f' and g' are determined as we describe in Section 4.2.4 in each direction. In 2D we only consider the first 4 cases and not the case where the characteristics form an expansion wave where $f'_L < 0$ and $f'_R > 0$.

4.3.3 Advection Equation for ϕ^*

In 2D we model the effects of irreversibility by solving an equation for ϕ^*, see Section 2.4.2. This is a linear advection equation

$$\phi_t^* + \boldsymbol{u} \cdot \nabla \phi^* = 0 \tag{4.42}$$

and is solved by using a first order upwind scheme. The finite differences are chosen depending on the characteristic velocities given by the components of the particle velocity. The scheme can be formulated as below.

$$\phi^{*n+1} = \phi^{*n} - k\left(\frac{|u_{i,j}| + u_{i,j}}{2} D^x_- \phi^*_{i,j} + \frac{|u_{i,j}| - u_{i,j}}{2} D^x_+ \phi^*_{i,j}\right) - k\left(\frac{|v_{i,j}| + v_{i,j}}{2} D^y_- \phi^*_{i,j} + \frac{|v_{i,j}| - v_{i,j}}{2} D^y_+ \phi^*_{i,j}\right) \tag{4.43}$$

4.3.4 Numerical Algorithm

The numerical algorithm is based on the algorithm described in Section 4.2.5 and extended to the 2D case. η^n does not only depend on ϕ^n but also on the shear rate $|\dot{\gamma}|^n$ which is computed using the velocity gradients at $t = t^{n-1}$. The yield pressure p_s depends also on ϕ^* and the convection equation for ϕ^*, (4.3.3) has to be solved at every time step.

The most time consuming step in the algorithm is the solution of the sparse linear algebraic problem of size $3N_xN_y$. As an alternative to the LU-factorization built into MATLAB®, we use the SuperLU package to factorize the matrix, see [6]. It contains a set of subroutines written in ANSI C for efficiently solving sparse linear systems. The package also include a MATLAB® MEX-file interface so the subroutines can be called direct from MATLAB®.

Chapter 5

Numerical Results

5.1 Introduction

In this section we report results from a set of numerical simulations and a convergence study of the numerical schemes.

Simulations are performed in order to investigate the effect of viscosity in the 1D model. The results are compared to the conclusions we made from the mathematical analysis of the 1D model in Section 3.2.1.

Also, 2D simulations are done to study the influence of shear and viscosity on the consolidation speed. From experiments a speed up in consolidation can be seen as a qualitative result of moving the bottom wall. However, this phenomenon is not very well captured by this model as can be seen from the computations.

5.2 Convergence Test - Order of Accuracy in Space

In 1D, the order of convergence in space is verified by a number of runs where the grid is successively refine as $\Delta y = h,\ h/2,\ h/4,\ h/8$ and $h/16$ where $h = 0.0025$. On each grid we solve (4.6)-(4.7) together with the boundary conditions given by (4.18) and (4.19). Since the coefficients and the source term depend on ϕ we let ϕ be a smooth function of y in order to avoid sharp gradients in the equations.

The results from the runs are shown in the Tables 5.5 and 5.2 below. Even if second order differences are used to discretize the system of equations we obtain less than second order convergence in v and p. This is due to the fact that we add artificial viscosity and that the boundary conditions for the pressure is implemented with a first order scheme.

In Table 5.5 we also present the value of the pressure correction term β introduced in Section 4.2.2. As predicted this is no larger than round-off and the pressure correction has little effect on the solution.

Let $\boldsymbol{v}^h$ and $\boldsymbol{p}^h$ denote the solutions computed at the spatial resolution h. We defined the discrete norm $\|\cdot\|_h$ as

$$\|\boldsymbol{v}\|_h^2 = h\sum_{j=1}^{N} |v_j|^2$$

h	$\|\boldsymbol{v}^h - \boldsymbol{v}^{h/2}\|_h$ 10^{-3}	$\frac{\|\boldsymbol{v}^{h/2}-\boldsymbol{v}^{h/4}\|_h}{\|\boldsymbol{v}^h-\boldsymbol{v}^{h/2}\|_h}$	conv rate	β 10^{-10}
0.0025	0.0174			0.001
		0.26	1.94	
0.00125	0.0045			-0.004
		0.31	1.70	
0.00063	0.0014			-0.006
		0.36	1.47	
0.00031	0.00051			-0.0539

Table 5.1. Order of accuracy for the velocity v using the numerical scheme (4.6)-(4.7). Note that β, which is related to the pressure correction, is a small number.

h	$\|\boldsymbol{p}^h - \boldsymbol{p}^{h/2}\|_h$	$\frac{\|\boldsymbol{p}^{h/2}-\boldsymbol{p}^{h/4}\|_h}{\|\boldsymbol{p}^h-\boldsymbol{p}^{h/2}\|_h}$	conv rate
0.0025	27.25		
		0.37	1.43
0.00125	10.06		
		0.38	1.40
0.00063	3.85		
		0.46	1.12
0.00031	1.75		

Table 5.2. Order of accuracy for the pressure p using the numerical scheme (4.6)-(4.7).

In 2D we solve (4.33)-(4.35) together with the boundary conditions given by (4.36)-(4.38). We use $h = 0.01$ and refine the grid as $\Delta y = \Delta x = h, h/2, h/8$. ϕ is a smooth function of (x, y) and η is a function of ϕ and multiplied with a factor of 100 in order to satisfy the stability restriction. The results are presented in the tables below. Here $\|\cdot\|_h$ is defined as

$$\|\boldsymbol{v}\|_h^2 = h^2 \sum_{i=1}^{N_x} \sum_{j=1}^{N_y} |v_{i,j}|^2$$

h	$\|\boldsymbol{u}^h - \boldsymbol{u}^{h/2}\|_h$	$\frac{\|\boldsymbol{u}^{h/2} - \boldsymbol{u}^{h/4}\|_h}{\|\boldsymbol{u}^h - \boldsymbol{u}^{h/2}\|_h}$	conv rate
0.01	0.2856		
		0.3876	1.37
0.005	0.1107		
		0.4554	1.13
0.0025	0.054		

Table 5.3. Order of accuracy for the velocity component u.

h	$\|\boldsymbol{v}^h - \boldsymbol{v}^{h/2}\|_h$	$\frac{\|\boldsymbol{v}^{h/2} - \boldsymbol{v}^{h/4}\|_h}{\|\boldsymbol{v}^h - \boldsymbol{v}^{h/2}\|_h}$	conv rate
0.01	0.2520		
		0.2660	1.91
0.005	0.0670		
		0.3230	1.63
0.0025	0.0217		

Table 5.4. Order of accuracy for the velocity component v.

h	$\|\boldsymbol{p}^h - \boldsymbol{p}^{h/2}\|_h$ 10^8	$\frac{\|\boldsymbol{p}^{h/2} - \boldsymbol{p}^{h/4}\|_h}{\|\boldsymbol{p}^h - \boldsymbol{p}^{h/2}\|_h}$	conv rate	β
0.01	2.723			$1.044 \cdot 10^{-14}$
		0.4684	1.09	
0.005	1.276			$4.709 \cdot 10^{-14}$
		0.5191	0.946	
0.0025	0.662			$-8.768 \cdot 10^{-13}$

Table 5.5. Order of accuracy for the pressure p. The pressure correction coefficient β is of round-off size.

5.3 The Effect of Viscosity in 1D

In the classical 1D model, studied by [2], [8] among others, the viscous stresses have been neglected. In [2] it is motivated by the fact that they consider suspensions where the inter particle forces dominate the viscous stresses. In the notation introduced in Section 2.3

$$\frac{\tau_0}{P_{s0}} \ll 1.$$

where $\tau_0 = \eta(\phi_0, |\dot{\gamma}_0|)\dot{\gamma}$, with $|\dot{\gamma}_0|$ a representative value of the shear rate. The experimental data on industrial sludge, see Fig 2.4, indicates a shear-thinning behavior and estimates of shear rate or τ_0 become difficult. For some cases, τ_0 may be large in relation to the interparticle force, and it is not obvious that the viscous stresses can be neglected.

This is illustrated by the mathematical analysis of the equations made in Section 3.2.1, where we show that for small viscosity, the consolidation speed is determined by the size of the permeability. When the viscosity increases, the viscous stresses become more important and finally they alone determine the sedimentation rate. Viscous forces are important only in boundary layers of thickness $\sqrt{\tilde{D}\eta}$ where $\tilde{D}$ is related to the effective Darcy coefficient. Consequently, if η is small, the boundary layer will be thin and the influence will be restricted to a domain close to the boundary which is also where the consolidation progresses most rapidly. But as η grows the boundary layer will become thicker and affect the solution in a larger domain.

To quantify the influence of viscosity we perform numerical experiments in 1D.

Let the viscosity be a function of ϕ only, $\eta(\phi) = K\phi^{3.4}$, where the dependence on ϕ is the same as in the experimental data on industrial sludge. K is a constant which determines the level of viscosity, see Fig 5.1. These levels can be interpreted as the variation of the viscosity with ϕ at different constant shear rates ranging from approximately $|\dot{\gamma}| = 6\ 1/s$ to $|\dot{\gamma}| = 0\ 1/s$. However, the upper level is somewhat artificial in relation to this problem, since the experimental data on the viscosity, (2.30), predicts a maximum viscosity of the order $10^7\ Pas$ (zero shear rate).

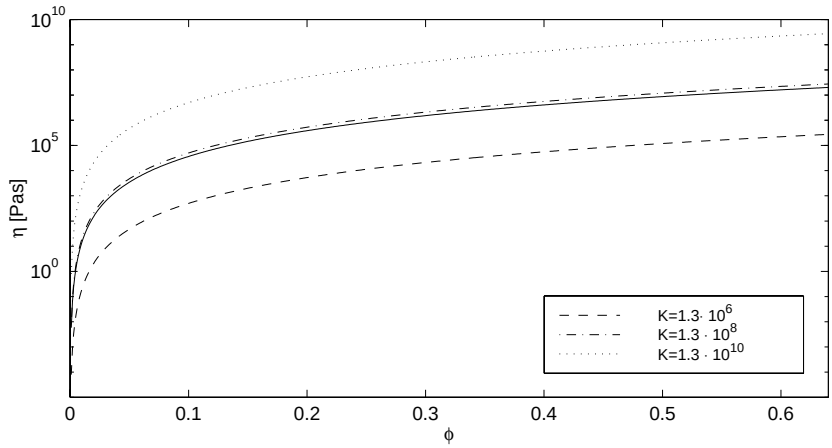

Figure 5.1. $\eta(\phi) = K\phi^{3.4}$ Different levels of viscosity used in the computations. These levels can be seen as the viscosity as a function of ϕ at different shear rates. The solid line represents $\eta(\phi)$ with $|\dot{\gamma}| \to 0$ in (2.30)

The permeability and the yield pressure are the models in Section 2.4. The gravity is $G = 1000\ m/s^2$ in a closed container of height $H = 0.1\ m$. The density difference between the solid phase and the liquid phase is $(\rho_s - \rho_f) = 1000\ kg/m^3$. The solution is computed until $t = 500\ s$. The space step size $h = 1.0 \cdot 10^{-3}\ m$ and the time step $k = 0.1\ s$.

The results for the three levels of viscosity are presented in Figures 5.2 and 5.3. It clearly shows that when the viscosity increases the viscous stresses become more important and will finally influence the time scale of the problem. In Figure 5.3 the velocity field has been plotted for the three different viscosities. The predicted increase of the boundary layer thickness can be seen at the bottom of the container. The velocity profile at the top of the container is not representative since there are no particles left, only clear fluid. But it provides information about the particle speed at the interface between the clear fluid and the overburden. The overburden is defined as a domain where the concentration is constant and equal to the initial concentration.

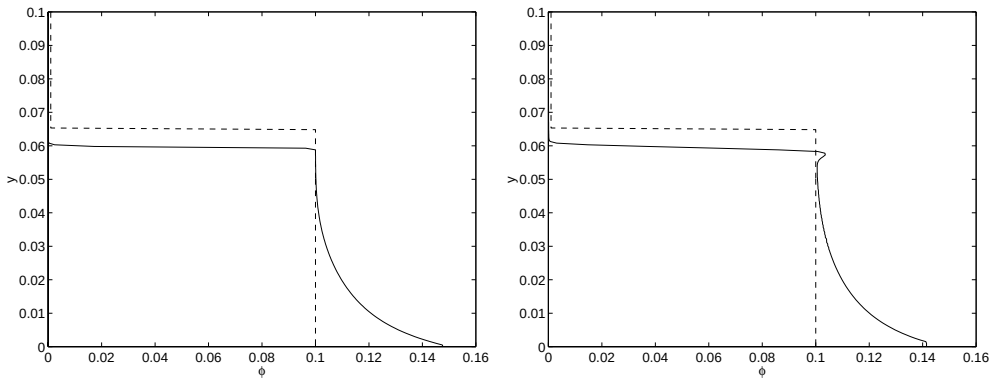

(a) $K = 1.3 \cdot 10^6$ Pas

(b) $K = 1.3 \cdot 10^8$ Pas

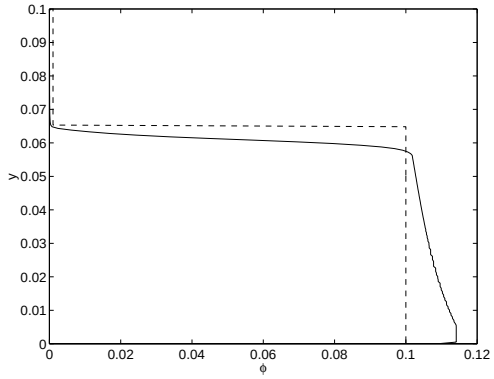

(c) $K = 1.3 \cdot 10^{10}$ Pas

Figure 5.2. The concentration ϕ at $t = 500s$ using different levels of viscosity given by the constant K, (solid line) compared to the initial profile (dashed line).

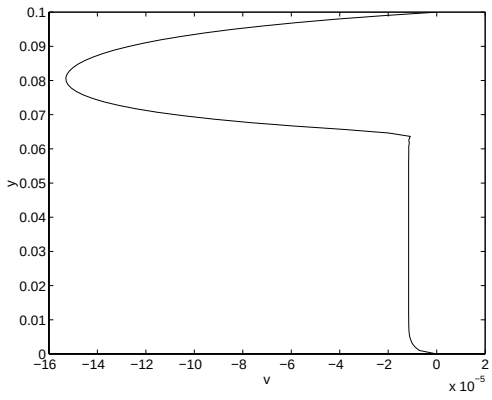

(a) $K = 1.3 \cdot 10^6$ Pas, $\delta = 2.2 \cdot 10^{-4}$ m

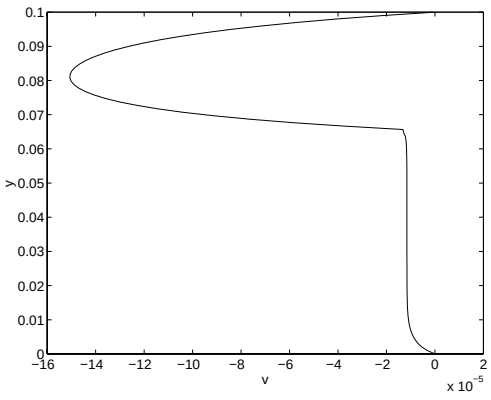

(b) $K = 1.3 \cdot 10^8$ Pas, $\delta = 0.0023$ m

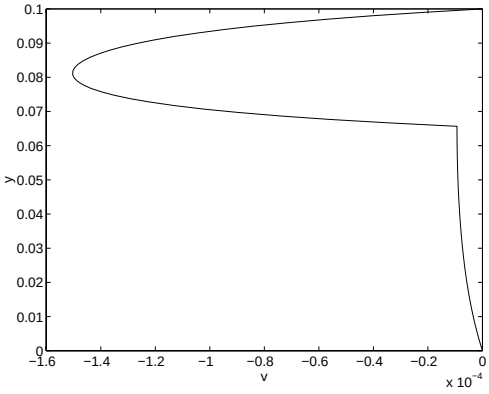

(c) $K = 1.3 \cdot 10^{10}$ Pas, $\delta = 0.024$ m

Figure 5.3. The velocity profile at $t = 10s$ using the different levels of viscosity. δ is the predicted size of the boundary layer thickness.

To conclude, we also compare our solutions with the classical 1D model, [8]. The computations use the same material data as above at a fixed level of viscosity. Computations until $t = 50000$ seconds, yield the following results presented in Figure 5.4. It show that the solutions agree well and in this case viscosity is negligible. The results also imply that there are no long time effects of the viscosity.

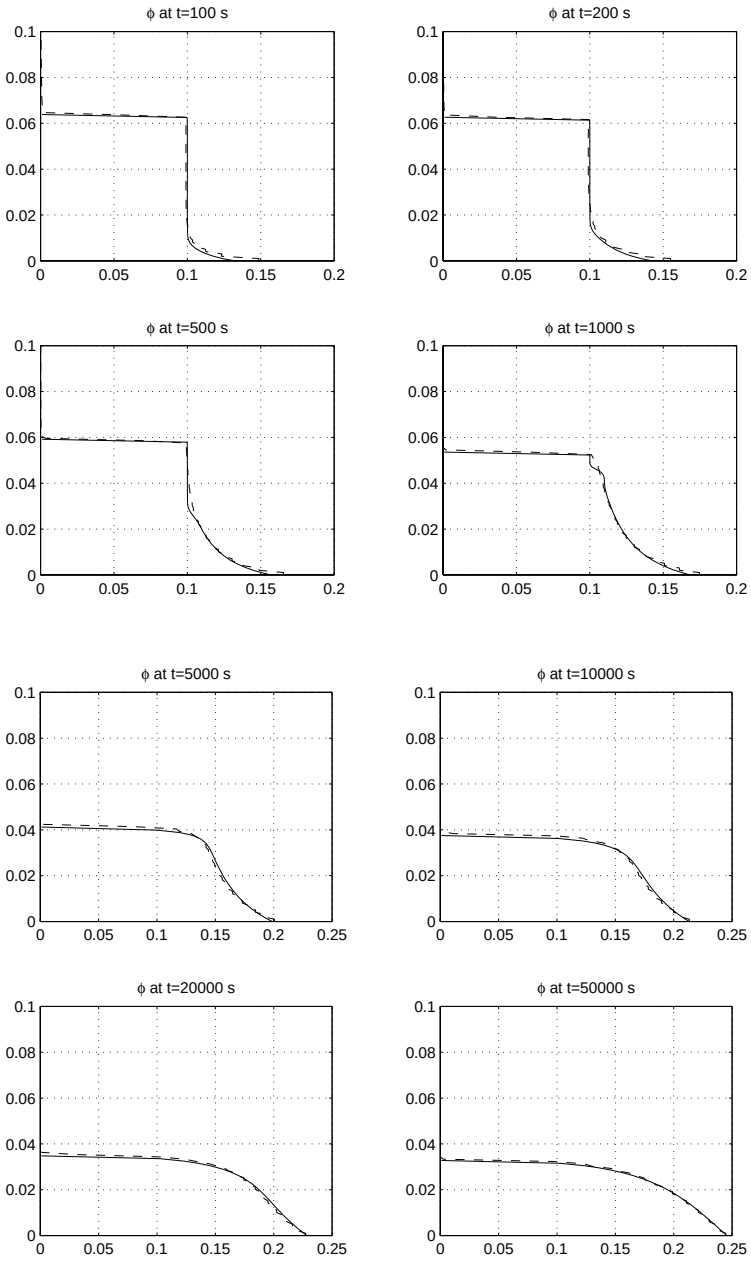

Figure 5.4. ϕ computed at different times using the 1D classical model (solid line) and the 1D viscous model (dashed line)

5.4 Effects of Shear in 2D

To investigate the effect of shear and other parameters on the consolidation, numerical computations are performed in 2D. The suspension is confined to a closed box of size $H \times H$. It consolidates due to a gravity field directed towards the bottom of the box, see Figure 4.6. Shear is induced by a movement of the bottom wall to the right with a constant speed.

A comparison between a shear thinning viscosity model and a viscosity that only depends on the concentration is also made. For this case, the shear thinning has only small influence on the mean concentration as s function of time.

The results from the simulations are presented below.

The constitutive relations involved in the computations are all discussed in section 2.4 and Section 3.1 . The mixture viscosity is given by either equation (5.1) or (5.3) depending on the test case. Other physical parameters in the model related to the suspension and the geometry are:

- Density difference between the phases $\Delta\rho = 1000\ kg/m^3$
- Fluid viscosity $\mu = 10^{-3}\ Pas$
- Box size $H = 0.1\ m$

Initially the box is filled up to $0.065\ m$ with a uniform concentration $\phi_0 = 0.1$. The rest of the box is clear fluid.

The amount of artificial viscosity added should be minimized. We increase the permeability, (2.25) by a factor of 100 and use a refined grid close to the bottom wall to perform computations without artificial viscosity. The increase in permeability will change the time scale of the problem and the width of the boundary layer.

The numerical parameters used in the computations are:

- $N_x = 40$, $N_y = 40$
- $c_\eta^u = 0$ and $c_\eta^v = 0$, no artificial viscosity
- $\Delta t = 0.05\ s$

where Δt is constant during the computations and is chosen to fulfill the CFL condition based on the initial fall speed.

5.4.1 The Effect of Bottom Wall Speed

In the experiment the gravity force, $G = 10000\ m/s^2$. Three different wall speeds are used in the computations: $0\ m/s$ (1D), $0.001\ m/s$ and $0.01\ m/s$. The viscosity is

$$\eta(\phi) = 1.3 \cdot 10^6 \phi^{3.4} \tag{5.1}$$

corresponding to a constant shear rate of approximately $6s^{-1}$ in the shear thinning model, see Figure 5.5.

Figure 5.6 shows the mean value, $\bar{\phi}$, of the concentration as a function of time. The mean value of ϕ is defined as

$$\bar{\phi} = \frac{1}{A_c} \int_{A_c} \phi dA_c \tag{5.2}$$

where A_c is the area for which ϕ is larger than a threshold value, $\phi_c = 0.05$.

In Figure 5.6 we observe that the maximum mean value of the concentration is obtained by 1D consolidation and moving the wall slows down the process. A large wall speed will set up a flow that is dominated by a divergence free velocity field and the consolidation will be slow. Figure 5.7 clearly shows that when the velocity is small the process is dominated by gravity and compression forces and the behavior is essentially 1D. And as the wall speed increases the viscous forces begin to dominate the process and the consolidation speed is slower.

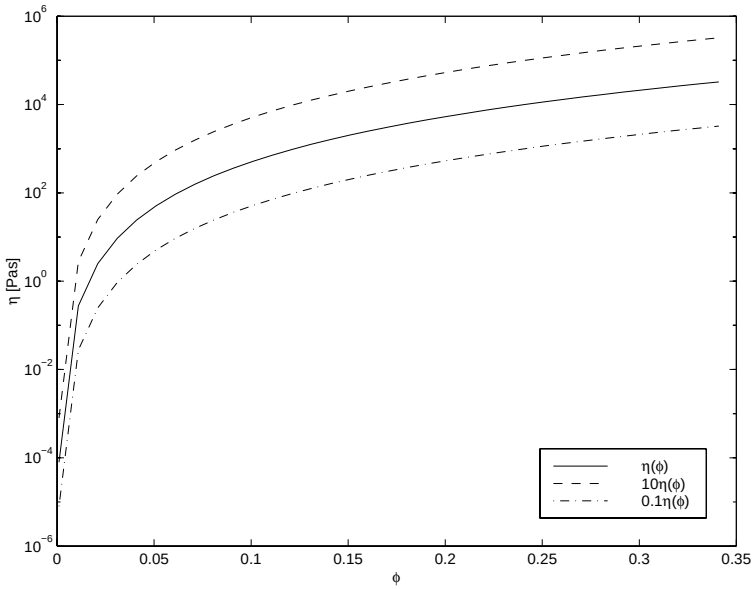

Figure 5.5. The viscosity as a function of ϕ only. It can be compared to a shear rate dependent viscosity at different constant shear rates. Solid line: $|\dot{\boldsymbol{\gamma}}| = 6s^{-1}$ Dashed line: $|\dot{\boldsymbol{\gamma}}| = 0.5s^{-1}$ Dash dotted line: $|\dot{\boldsymbol{\gamma}}| = 50s^{-1}$

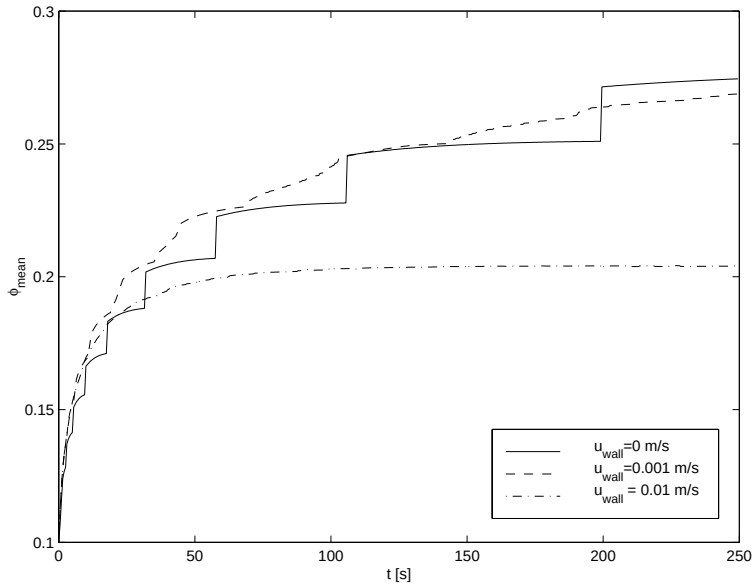

Figure 5.6. The mean concentration as a function of time for different wall speeds. $u_{wall} = 0, 0.01, 0.001m/s$. The viscosity is a function of ϕ only given by equation (5.1)

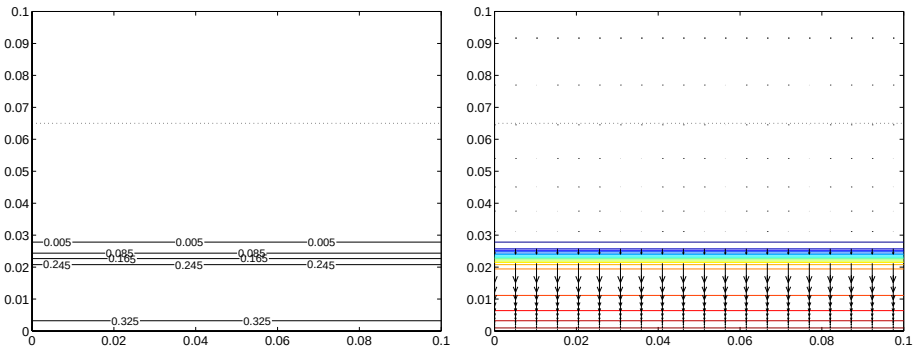

(a) $u_{wall} = 0m/s$ (b) $u_{wall} = 0m/s$

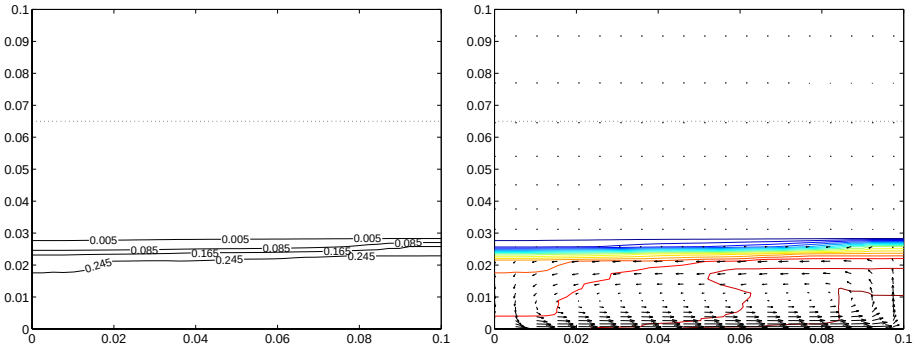

(c) $u_{wall} = 0.001m/s$ (d) $u_{wall} = 0.001m/s$

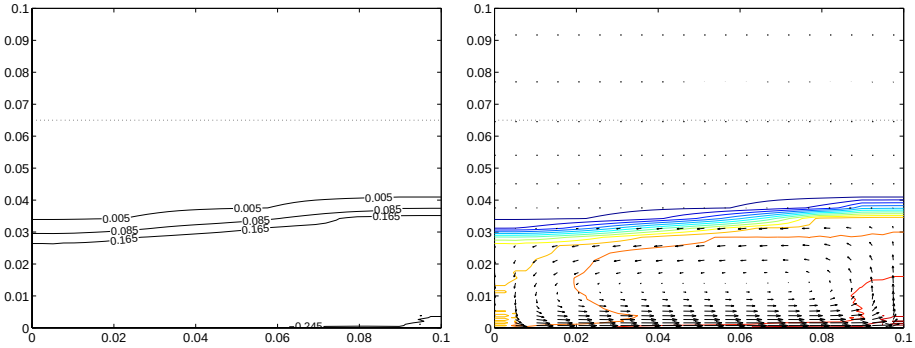

(e) $u_{wall} = 0.01m/s$ (f) $u_{wall} = 0.01m/s$

Figure 5.7. Concentration contours at the end time t=250 s. The computations were performed with three different bottom wall speeds and $G = 10000m/s^2$. The viscosity is a function of ϕ only, given by equation (5.1). The dotted line indicate the initial condition. In the right figures the arrows indicate the volume solid-flux.

In Figure 5.8 we show the time history of the consolidation process. We see that it consolidates fast in the beginning of the process and that it is essentially a 1D process.

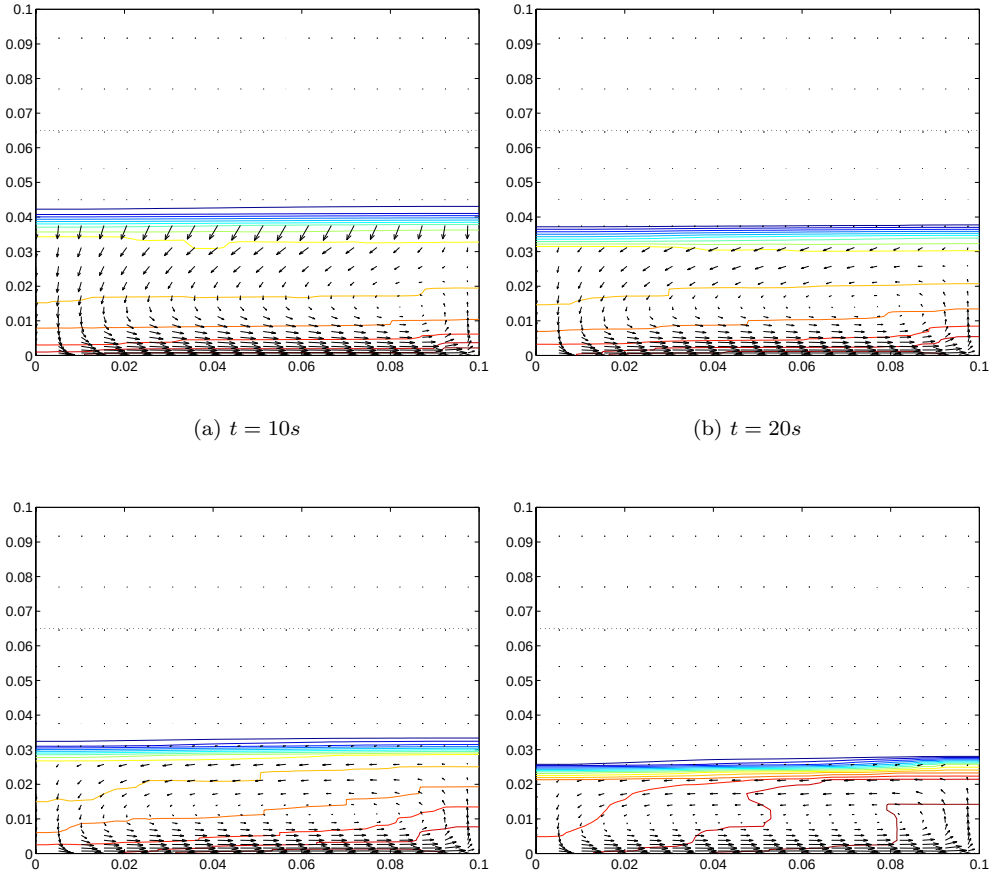

(a) $t = 10s$ (b) $t = 20s$

(c) $t = 50s$ (d) $t = 250s$

Figure 5.8. Concentration contours at t=10, 20, 50 and 250 s. With $u_{wall} = 0.001m/s$

5.4.2 Effect of Shear Thinning

The shear thinning model, (5.3), gives a larger "over-all-viscosity" than in the previous cases, (5.4.1). The reason is as follows. The viscosity (5.1) corresponds to a shear rate dependent viscosity at a constant shear rate of approximately 6 s^{-1}, see Figure 5.5. But the shear rates in the actual computations turn out to be $\approx 0.5\ s^{-1}$ and only larger locally towards the bottom.

$$\eta(\phi, |\dot{\gamma}|) = 9.15 \cdot 10^7 \phi^{3.4} \left(1 + \frac{|\dot{\gamma}|}{0.05}\right)^{-0.9} \tag{5.3}$$

The same computations are performed as above with $G = 10000\ m/s^2$ and different wall speeds. The influence of shear thinning on the mean concentration as a function of time can be studied by comparing Figure 5.9 and 5.6. In both cases the 1D consolidation yields the highest mean concentration. A slightly higher mean concentration is obtained using $u_{wall} = 0.01\ m/s$ than $0.001\ m/s$. $u_{wall} = 0.1\ m/s$, however, is "large" and slows down the consolidation.

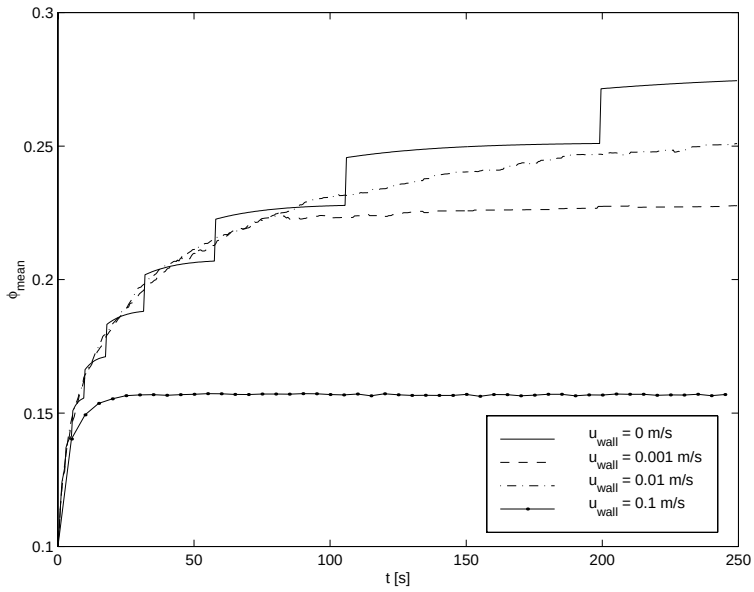

Figure 5.9. The mean concentration as a function of time using different wall speeds with shear thinning.

In Figure 5.10 we observe that the suspension behaves differently from the previous case, for comparison see Figure 5.7. With shear thinning the suspension tends to "climb up" the right side wall and due to the high viscosity behave more solid-like.

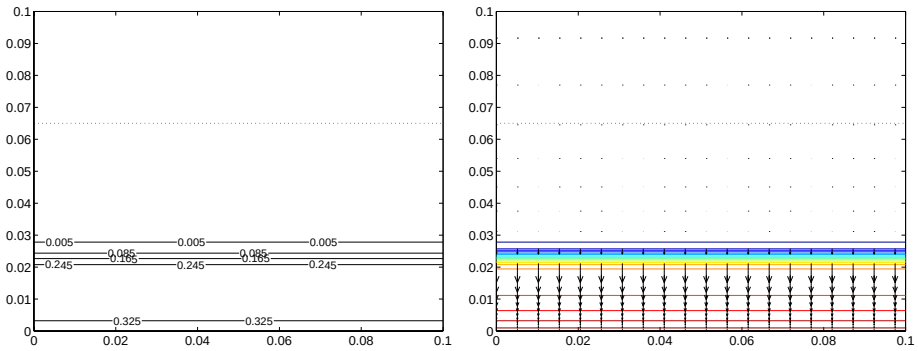

(a) $u_{wall} = 0m/s$ (b) $u_{wall} = 0m/s$

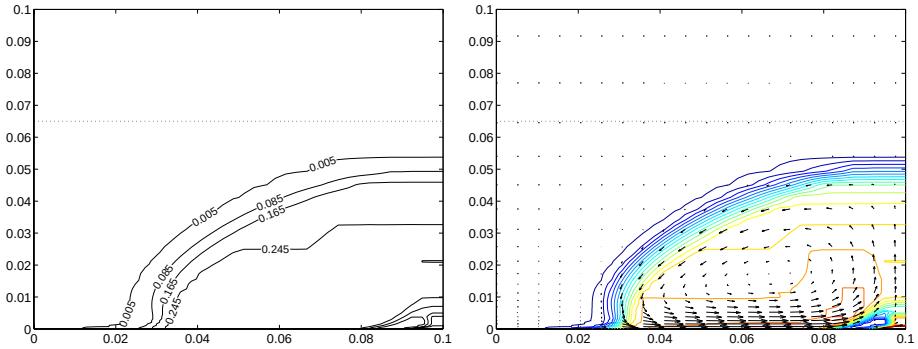

(c) $u_{wall} = 0.001m/s$ (d) $u_{wall} = 0.001m/s$

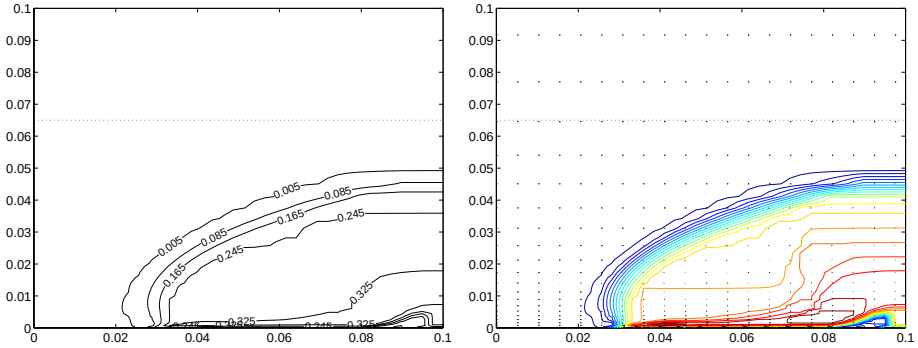

(e) $u_{wall} = 0.01m/s$ (f) $u_{wall} = 0.01m/s$

Figure 5.10. Concentration contours at the end time t=250 s with shear thinning. In the figures on the right hand side we show the volume solids-flux as arrows.

Figure 5.11 show the solution at different times. Also in this case the suspension consolidates fast in the beginning of the process. After a while the viscosity sets up a large rotating velocity field which does not contribute to the consolidation.

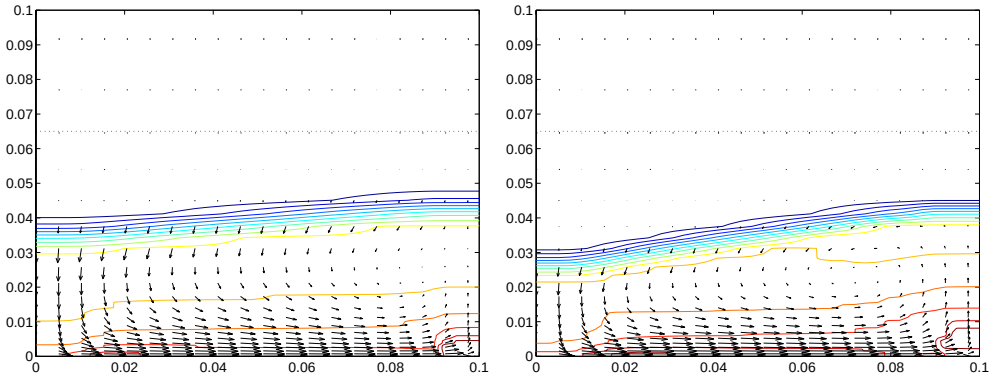

(a) $t = 10s$ (b) $t = 20s$

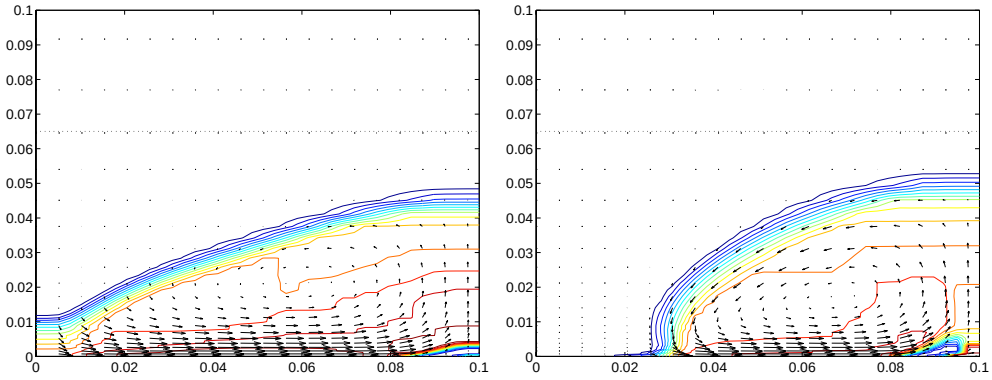

(c) $t = 50s$ (d) $t = 250s$

Figure 5.11. Concentration contours at t=10, 20, 50 and 250 s. With $u_{wall} = 0.001m/s$, $G = 10000m/s^2$

To study the influence of the size of the viscosity equation (5.1) is scaled with 10 and 0.1, see Figure 5.5. The results can be seen in Figure 5.12. We see that the boundary layer grows with increasing viscosity. And a large viscosity yields a negative effect on the consolidation process and leads to a lower mean value of the concentration, see also Figure 5.13. In Figure 5.13 the mean value of ϕ is also plotted for the case where we used a shear thinning model. Even though the "over-all-viscosity" in that case is of the same order as $10\eta(\phi)$ the mean concentration is much higher. One reason could be that locally towards the bottom the viscosity is much lower.

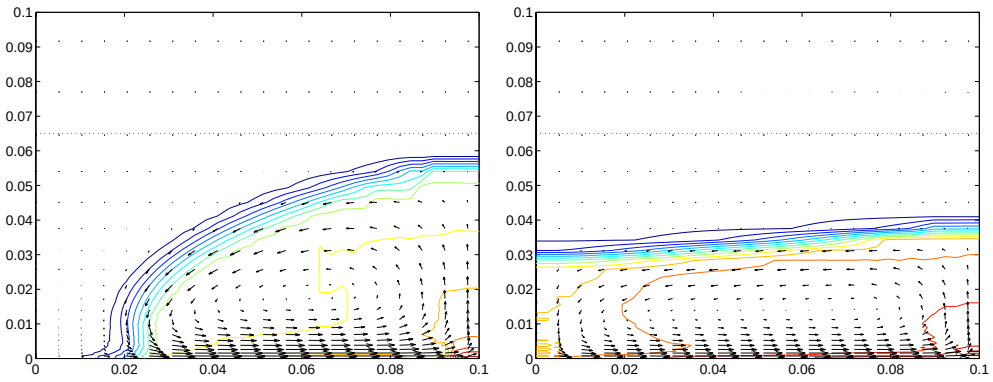

(a) $\eta = 10\eta(\phi)$ (b) $\eta = \eta(\phi)$

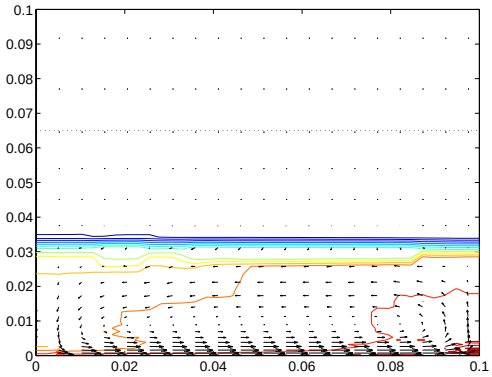

(c) $\eta = 0.1\eta(\phi)$

Figure 5.12. Concentration contours at the end time t=250 s. The computations were performed with different viscosities models and sizes $\eta = 10\eta(\phi)$, $\eta = \eta(\phi)$ and $\eta = 0.1\eta(\phi)$. $G = 10000m/s^2$ and $u_{wall} = 0.01m/s$.

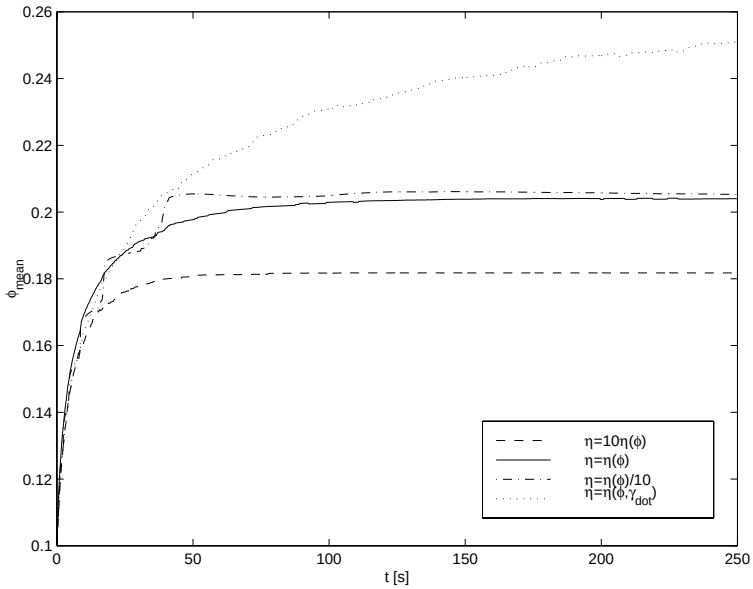

Figure 5.13. The mean concentration as a function of time for different viscosities, $\eta = \eta(\phi)$.$G = 10000m/s^2$ and $u_{wall} = 0.01m/s$. Dotted line: viscosity is a function of the shear rate and concentration.

Chapter 6

Conclusions

We study a model of a consolidation process of a strongly flocculated suspension. This is done from a mathematical and a numerical point of view. A commonly used model of a multi phase flow is the Eulerian two fluid model which is applicable to fluid-particle flow. By scale analysis we motivate a simplification: In a gravity dominated process the inertial terms can be neglected. This leads to a reduction of the model since the fluid velocity field can be eliminated.

Consolidation processes for dense suspensions are often modeled as one-dimensional. Important effects of shearing motion are then neglected. In this work we have concentrated on models in 1D and 2D for which the material data can be supplied by relatively simple measurement techniques. In particular, there is no explicit empirical modeling of material fluxes due to shear or concentration gradients such as in [15] and [20] but there is nevertheless an influence of shear.

It is easily estimated in the 1D model: A large viscosity increases the time scale, but for many applications the neglect of viscosity is justified as is customarily done in the classical model. This is illustrated by numerical experiments.

The 2D case is much more involved. The mathematical estimates in L_2-norms are tractable only when variations in coefficients are neglected. The simulations are also more difficult and time-consuming. The influences of the bottom wall velocity and viscosity model are illustrated by a series of numerical experiments.

Various spatial difference schemes and boundary condition treatment for the velocity equations were investigated. The intrinsic length-scale of the problem, $H = \sqrt{D\eta}$ where η is the viscosity and D is the Darcy coefficient, can be small and artificial viscosity has to be applied. A priori, fixed grading of the mesh is also effective for the layer at the bottom of the box.

The conservation law for the concentration is strongly non-linear and displays an important moving internal layer where the concentration drops rapidly to zero at the clear fluid interface. The numerical scheme is inspired by the Godunov scheme.

The current version of the simulation program would probably benefit from the introduction of a high-resolution scheme for the conservation laws and a higher order time-stepping method. The limiting factor for the spatial resolution is the direct linear solver. Iterative schemes such as pre-conditioned GMRES, QMR, and CGS were briefly

investigated with limited success. Further experiments with pre-conditioners combined with multi-grid acceleration are necessary.

Bibliography

[1] T.B. Anderson and R. Jackson. Fluid mechanical description of fluidized beds. *Industrial and Engineering Chemistry Fundamentals*, 6:527–538, 1967.

[2] F.M. Auzerais, R.J. Jackson, and W.B. Russel. The resolution of shocks and the effect of compressible sediments in transient settling. *J. of Fluid Mechanics*, 195:437–462, 1988.

[3] L. Bergström. *Surface and Colloid Chemistry in Advanced Ceramics Processing*, chapter 5, Rheology of Concentrated Suspensions. Marcel Dekker Inc, 1994.

[4] R.B. Bird, C.F. Curtiss, R.C. Armstrong, and O. Hassager. *Dynamics of Polymeric Liquids*. Wiley Interscience, 1987.

[5] R. Bürger and F. Concha. Mathematical model and numerical simulation on the settling of flocculated suspensions. *Int. J. of Multiphase Flow*, 24:1005–1023, 1998.

[6] J.W. Demmel*, J.R. Gilbert, and X.S. Li. Superlu users' guide. Technical report, *Computer Science Division, University of California, Berkley, USA, 1997.

[7] S. Diehl. *Conservation Laws with Application to Continuous Sedimentation*. Iisrn lutfd, Department of Mathematics,Lund Institute of Technology, P.O. Box 118, S-221 00 Lund , SWEDEN, May 1995.

[8] M. Dorobantu. One-dimensional consolidation models. Trita, Department of Numerical Analysis and Computing Science, Royal Institute of Technology, 100 44 Stockholm, SWEDEN, 1997.

[9] D.A. Drew. Mathematical modeling of two-phase flow. *Ann. Rev. Fluid Mechanics*, 15:261–291, 1983.

[10] H. Enwald, E. Peirano, and A-E. Almstedt. Eulerian two-phase flow theory applied to fluidization. *Int. J. of Multiphase Flow*, 22:21–46, 1996.

[11] C.A.J. Fletcher. *Computational Techniques for Fluid Dynamics, vol I-II*. Springer-Verlag, 1991.

[12] M. D. Green. *Characterisation of Suspensions in Settling and Compression*. PhD thesis, Department of Chemical Engineering, University of Melbourne, Parkville, Victoria 3052, Australia, June 1997.

[13] K. Walters H.A. Barnes, J.F. Hutton. *An Introduction to Rheology*. Elsevier Science Publisher, 1989.

[14] M. Ishii. *Thermo-Fluid Dynamic Theory of Two-Phase Flow*. Eyrolles, 1975.

[15] D. Leighton and A. Acrivos. The shear-induced migration of particles in concentrated suspensions. *J. of Fluid Mechanics*, 181:415–439, 1987.

[16] R.J. LeVeque. *Numerical Methods for Conservations Laws*. Birkhäuser Verlag, Basel, 1992.

[17] E. Pärt-Enander and A. Sjöberg. *Användarhandledning för MATLAB 5*. Uppsala Universitet, 1998.

[18] A.E. Scheidegger. *The Physics of Flow Through Porous Media*. University of Toronto Press, 1963.

[19] J.C. Strikwerda. *Finite Difference Schemes and Partial Differential Equations*. Wadsworth and Brooks/Cole Advanced Books and Software, 1989.

[20] S.R. Subia, M.S. Ingber L.A. M.S. Ingber, L.A. Mondy, S.A. Altobelli, and A.L. Graham. Modelling of concentrated suspension using a continuum constitutive equation. *J. of Fluid Mechanics*, 373:193–219, 1998.

[21] R. Temam. *Navier-Stokes Equations*. North-Holland Publishing Company, 1979.

[22] J.F. Thompson, Z.U.A. Warsi, and C.W. Mastin. *Numerical Grid Generation, Foundations and Applications*. Elsevier Science Publishing Co., Inc., 1985.

[23] M. Ungarish. *Hydrodynamics of Suspensions*. Springer-Verlag, 1993.

[24] J. Yström. *On the Numerical Modeling of Concentrated Suspensions and of Viscoelastic Fluids*. Trita–na–9603, Department of Numerical Analysis and Computing Science, Royal Institute of Technology, 100 44 Stockholm, SWEDEN, September 1996.

[25] S. Zahrai. *On the Fluid Mechanics of Twin-Wire Formers*. PhD thesis, Department of Mechanics, Royal Institute of Technology, 100 44 Stockholm, SWEDEN, October 1997.